L
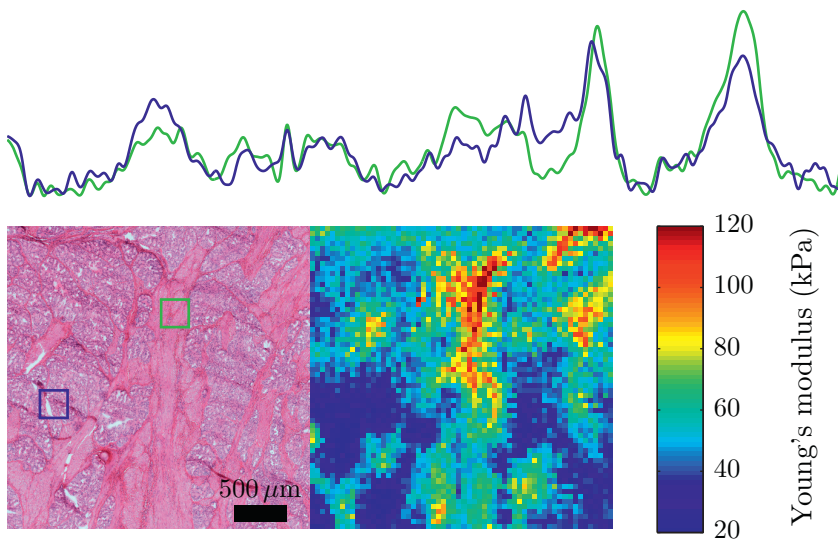
Combining the Tactile Resonance Method and Raman Spectroscopy for Tissue Characterization towards Prostate Cancer Detection

Stefan Candefjord

LULEÅ
UNIVERSITY
OF TECHNOLOGY

Combining the Tactile Resonance Method and Raman Spectroscopy for Tissue Characterization towards Prostate Cancer Detection

Stefan Candefjord

Dept. of Computer Science, Electrical and Space Engineering
Luleå University of Technology
Luleå, Sweden

To the memory of my father, Jan-Åke Candefjord

ABSTRACT

Prostate cancer (PCa) is the most common male cancer in Europe and the US, and only lung and colorectal cancer have a higher mortality among European men. In Sweden, PCa is the most common cause of cancer-related death for men.

The overall aim of this thesis was to explore the need for new and complementary methods for PCa detection and to take the first step towards a novel approach: combining the tactile resonance method (TRM) and Raman spectroscopy (RS). First, the main methods for PCa detection were reviewed. Second, to establish a robust protocol for RS experiments in vitro, the effects of snap-freezing and laser illumination on porcine prostate tissue were studied using RS and multivariate statistics. Third, measurements on porcine and human tissue were performed to compare the TRM and RS data via multivariate techniques, and to assess the accuracy of classifying healthy and cancerous tissue using a support vector machine algorithm.

It was concluded through the literature review that the gold standard for PCa detection and diagnosis, the prostate specific antigen test and systematic biopsy, have low sensitivity and specificity. Indolent and aggressive tumors cannot be reliably differentiated, and many men are therefore treated either unnecessarily or too late. Clinical benefits of the state–of–the–art in PCa imaging – advanced ultrasound and MR techniques – have still not been convincingly shown. There is a need for complementary and cost-effective detection methods. TRM and RS are promising techniques, but hitherto their potential for PCa detection have only been investigated in vitro.

In the RS study no evidence of tissue degradation due to 830 nm laser illumination at an irradiance of $\sim 3 \cdot 10^{10}$ W m^{-2} were found. Snap-freezing and subsequent storage at $-80\,^{\circ}$C gave rise to subtle but significant changes in Raman spectra, most likely related to alterations in the protein structure. The major changes due to PCa do not seem to be related to the protein structure, hence snap-freezing may be applied in our experiments.

The combined measurements on porcine and human prostate tissue showed that RS provided additional discriminatory power to TRM. The classification accuracy for healthy porcine prostate tissue, and for healthy and cancerous human prostate tissue, was $> 73\%$. This shows the power of the support vector machine applied to the combined data.

In summary, this work indicates that an instrument combining TRM and RS is a promising complementary method for PCa detection. Snap-freezing of samples may be used in future RS studies of PCa. A combined instrument could be used for tumor-border demarcation during surgery, and potentially for guiding prostate biopsies towards lesions suspicious for cancer. All of this should provide a more secure diagnosis and consequently more efficient treatment of the patient.

CONTENTS

ACKNOWLEDGMENTS

☞ All my friends and colleagues at the Dept. of Computer Science, Electrical and Space Engineering. You have made my time as doctoral student very amusing. I have laughed for days after many of our discussions during coffee breaks. Many of you have also contributed with valuable discussions and collaborative work in different courses. I would especially like to thank Johan Borg for all valuable tips about performing measurements and developing the experimental setup.

☞ The EU Objective 2, Northern Sweden, for supporting my work, and the Kempe Foundation for funding much of our laboratory equipment.

☞ The study was performed within the CMTF network.

☞ My warmest thanks to my family and my girlfriend, Linda, for all your love and support.

Luleå, May 9, 2011
Stefan Candefjord

Part I

Chapter 1

Original Papers and My Contributions

In this thesis the following peer-reviewed papers are included and referred to by their Latin letters. My contributions to these papers are shown in Table 1.1.

(A) S. Candefjord, K. Ramser & O. A. Lindahl, "Technologies for localization and diagnosis of prostate cancer", *Journal of Medical Engineering & Technology*, vol. 33, pp. 585–603, 2009.

(B) S. Candefjord, K. Ramser & O. A. Lindahl, "Effects of snap-freezing and near-infrared laser illumination on porcine prostate tissue as measured by Raman spectroscopy", *Analyst*, vol. 134, pp. 1815–1821, 2009.

(C) S. Candefjord, M. Nyberg, V. Jalkanen, K. Ramser & O. A. Lindahl, "Combining fibre optic Raman spectroscopy and tactile resonance measurement for tissue characterization", *Measurement Science & Technology*, vol. 21, 125801 (8 pp.), 2010.

(D) S. Candefjord, Y. Murayama, M. Nyberg, J. Hallberg, K. Ramser, B. Ljungberg, A. Bergh & O. A. Lindahl, "Combining scanning haptic microscopy and fiber optic Raman spectroscopy for tissue characterization", Submitted to *Medical & Biological Engineering & Computing*, May 2011.

Table 1.1: *The contributions made by Stefan Candefjord to Papers A–D. 1 = main responsibility, 2 = Contributed to high extent, 3 = Contributed.*

Part	A	B	C	D
Idea and formulation of the study	2	3	2	2
Experimental design	-	1	2	2
Performance of experiments	-	1	2	1
Data analysis	1	1	2	1
Writing of manuscript	1	1	1	1

CHAPTER 2

Other Publications of Relevance

Other publications of relevance, but not included in this thesis, are listed below.

(1) S. Candefjord, "Combining a resonance and a Raman sensor: towards a new method for localizing prostate tumors in vivo", Technical Report, ISSN: 1402-1536, Luleå University of Technology, Luleå, Sweden, 2007.

(2) S. Candefjord, K. Ramser and O. A. Lindahl, "Towards new sensors for cancer detection in vivo, a handheld detector combining a fibre-optic Raman probe and a resonance sensor", Conference Abstract, Looking Skin Deep – Clinical and Technical Aspects of Skin Imaging, 1st workshop by Göteborg Science Centre for Molecular Skin Research, Göteborg, Sweden, 2007.

(3) S. Candefjord, K. Ramser and O. A. Lindahl, "En ny metod för att lokalisera och diagnostisera prostatacancer", Conference Abstract, Medicinteknikdagarna 2007, Örebro, Sweden, 2007.

(4) S. Candefjord, K. Ramser and O. A. Lindahl, "Effects of snap-freezing and laser illumination of tissue on near-infrared Raman spectra of porcine prostate tissue", Conference Abstract, SPEC 2008, Shedding Light on Disease: Optical Diagnosis for the New Millennium, São José dos Campos, São Paulo, Brazil, 2008.

(5) S. Candefjord, M. Nyberg, V. Jalkanen, K. Ramser & O. A. Lindahl, "Evaluating the Use of a Raman Fiberoptic Probe in Conjunction with a Resonance Sensor for Measuring Porcine Tissue in vitro", O. Dössel & W. C. Schlegel (ed.), WC 2009, IFMBE Proceedings, vol. 25, no. 7, pp. 414–417, 2009.

(6) S. Candefjord, "Towards new sensors for prostate cancer detection – combining Raman spectroscopy and resonance sensor technology", Licentiate Thesis, ISBN 978-91-86233-59-4, Luleå University of Technology, Luleå, Sweden, 2009.

(7) S. Candefjord, M. Nyberg, V. Jalkanen, K. Ramser & O. A. Lindahl, "Kombinations-instrument för detektering av prostatacancer – korrelation mellan resonanssensor och fiberoptisk Ramanprobe", Conference Abstract, Medicinteknikdagarna 2009, Västerås, Sweden, 2009.

(8) S. Candefjord, K. Ramser & O. A. Lindahl, "Kombinationsinstrument för detektering av prostatacancer – mätningar på snitt av grisprostata med resonanssensor och fiberoptisk Ramanprobe", Conference Abstract, Medicinteknikdagarna 2010, Umeå, Sweden, 2010.

CHAPTER 3

Abbreviations

BPH   benign prostatic hyperplasia
HCA   hierarchical clustering analysis
MR   magnetic resonance
MRI   magnetic resonance imaging
MRSI   magnetic resonance spectroscopic imaging
MTS   micro tactile sensor
NIR   near-infrared
PBS   phosphate buffered saline
PC   principal component
PCA   principal component analysis
PCa   prostate cancer
PSA   prostate-specific antigen
PZT   lead zirconate titanate
RS   Raman spectroscopy
SHM   scanning haptic microscopy
SB   systematic biopsy
SVM   support vector machines
TRM   tactile resonance method

CHAPTER 4

Introduction

This chapter explains the problems prostate cancer poses to public health, describes the theory for the tactile resonance method and Raman spectroscopy, discusses pitfalls for in vitro experiments, and gives an insight into the mathematical tools that were used in this work.

4.1   General background

Prostate cancer (PCa) is the most common form of male cancer in the US and Europe [1, 2]. From the most recent data it is estimated that PCa caused almost $90\,000$ deaths in Europe in 2008, and only lung and colorectal cancer have a higher mortality among European men [1]. In the US it is the second leading cause of male death due to cancer [2], and the severity of the disease is strongly related to insurance status [3]. The incidence of PCa is expected to increase due to the aging population [4].

PCa is often indolent, more men die with the disease than from it. Considering the large risks for side effects such as impotence and incontinence after radical prostatectomy, i.e. surgical removal of the prostate, active surveillance may be the best option for patients with indolent tumors [5, 6]. On the other hand, to reduce PCa mortality, patients with aggressive tumors likely to metastasize must be treated early on [6]. Current clinical diagnostic tests, the prostate specific antigen (PSA) test, and multiple systematic biopsy (SB), miss many tumors and cannot reliably distinguish between indolent and aggressive PCa [7, 8]. As a consequence, many men are treated either unnecessarily or too late.

The prostate is a deep-sited organ with heterogeneous structure [9, 10]; that makes it difficult to recognize tumors using medical imaging techniques. Advanced techniques for ultrasound and magnetic resonance imaging (MRI) show relatively high sensitivity for PCa detection [11, 12]. However, benign lesions such as prostatitis and benign prostatic hyperplasia (BPH) often give false alarms [11, 12].

The major objective of PCa detection is a more precise disease characterization [13]. Today, there is a lack of information for deciding whether patients that undergo radical prostatectomy would benefit from additional therapy [14]. For high-risk patients further treatment with medical, radiation and/or chemotherapy may be useful [14, 15]. However, selecting appropriate patients upfront is challenging, and delaying adjuvant therapy until

there is evidence of cancer regrowth seems to decrease survival rates [14]. One reason that many patients suffer from cancer recurrence is failure to remove all cancerous tissue at surgery [16]. Positive surgical margins, i.e. cancer present on the surface of the dissected tissue, are found in up to 40% of patients [16, 17]. There is currently no accurate technique for analyzing the surgical margins during operation [16, 17]. Thus, it becomes challenging for surgeons to remove all cancerous tissue while avoiding damage leading to erectile dysfunction or incontinence [16]. New complementary methods for PCa detection and diagnosis are needed. This thesis takes the first steps towards a novel approach where two experimental techniques are combined, i.e. the tactile resonance method (TRM) and Raman spectroscopy (RS).

TRM was developed to mimic palpation, i.e. to feel the stiffness of a tissue using the fingers, and this is performed by physicians to find tissue abnormalities [18]. The stiffness of many organs are affected by diseases. Tumors are usually stiffer than healthy tissue and can be felt as hard nodules in, e.g. breast and prostate tissue. TRM gives an objective measure of the stiffness through frequency changes of a piezoelectric vibrating element. Several medical applications have been introduced, including measuring the stiffness of single cells to evaluate embryo quality and increase the success-rate of in vitro fertilization [18]. TRM is promising for breast and prostate cancer detection [18]. In vitro studies show that TRM can differentiate soft, healthy prostate tissue from PCa [19–21]. However, the sensitivity is currently insufficient to distinguish between tumors and relatively hard healthy tissue, such as sites with an accumulation of prostate stones.

RS measures the biochemical composition of tissue via laser illumination and analysis of the spectrum of the inelastically scattered light. Disease progression is reflected by changes in the molecular contents of tissue [22]. RS is very promising for a wide range of diagnostic applications [22]. Numerous in vitro studies show that RS can detect many types of cancers, including PCa, with high sensitivity and specificity [22–27]. Despite this high potential, few clinical implementations have emerged. The main reason is a lack of small, flexible and disposable RS fiber optic probes adequate for large clinical trials [28]. RS is very promising for distinguishing indolent and aggressive PCa [24, 25, 27, 29]. The disadvantages of RS are that current fiber optic probes have short penetration depth in tissue ($\sim$ 0.1 mm [30]), that surrounding light can interfere with the signal of interest, and that intense laser irradiation may damage tissue.

To combine TRM and RS could add up their strengths while minimizing the drawbacks associated with each technique. TRM constitutes a quick, gentle and deep-sensing method that could be used for swift scanning of the tissue. RS could provide complementary information for nodules suspected to be cancerous. In the first place, the combined instrument could be used to probe the surgical margins during radical prostatectomy. In the long term, it could potentially be used for minimally invasive localization and diagnosis of PCa.

In vitro studies are necessary for successful implementation of the combined instrument. To ascertain that the results are transferable to the in vivo situation, it is important that the experimental procedures preserve the native tissue characteristics. Possible degradation of tissue from, e.g. sample preservation and preparation methods, laser

irradiation, and dehydration during measurements, should be investigated.

This thesis gives a background to the difficulties of localizing and diagnosing PCa. It reviews the main methods for PCa detection in clinical use today, and discusses promising novelties that are being developed. The importance of robust in vitro study protocols is discussed, and the effects of snap-freezing and near-infrared laser (NIR) illumination on porcine prostate tissue are investigated using RS. An approach for combining the information from TRM and RS is developed and evaluated on measurements on porcine abdominal tissue. Finally, the accuracy of classification of healthy and cancerous prostate tissue is investigated in experiments on porcine and human samples using a novel experimental setup with a micro tactile sensor (MTS) and an RS fiberoptic probe.

4.2 The prostate

4.2.1 Anatomy and physiology

The prostate is an accessory sex gland whose function is to store and secrete a milky, slightly acidic fluid (pH ~ 6.5), which makes up about 25% of the volume of semen [31]. The gland is about the size of a golf ball and resembles a walnut in shape. It is situated inferior to the bladder, next to the rectal wall that is about 3 mm thick [32], and encircles the prostatic urethra (Figure 4.1). Many prostatic ducts lead the prostatic fluid into the urethra. The prostate is composed of glandular elements that are lined with epithelial cells that secrete prostatic fluid into the glandular lumen (cavity) [10]. The glandular elements are separated by stroma, a supportive framework that consists of smooth muscle tissue and other cellular components embedded in an extracellular matrix rich in collagen [31,33]. There are three anatomical zones in the prostate: the peripheral zone, the transitional zone and the central zone. The composition of the prostate tissue varies between the zones, e.g. the stroma is more or less compact with varying amounts of muscle tissue [10].

The prostate normally increases in volume during specific periods throughout a man's life. It grows rapidly from puberty until about age 30, remains at a stable size between age 30 and 45, after which it may begin to grow again [31]. The majority of men > 55 years develop BPH, a benign enlargement of the prostate [34]. The formation of prostate stones (corpora amylacea) in the lumen of the glandular elements, due to solidification of glandular secretions, is another common benign occurrence [35,36]. The stones are quite hard and contribute to tissue stiffness, although they make up only a small fraction of the tissue volume [19,37]. They are rarely present in cancerous tissue [36].

The functional role of prostatic fluid is not completely understood, but the following is known [31]:

❏ It participates in making the semen coagulate after ejaculation, which happens within five minutes (the role of coagulation is unknown).

❏ It contains protein-digesting enzymes, among them, PSA, which starts to liquefy the semen at 10–20 minutes after ejaculation. This facilitates the movement of sperm through the cervix.

This shows the prostate and nearby organs.

This shows the inside of the prostate,
urethra, rectum, and bladder.
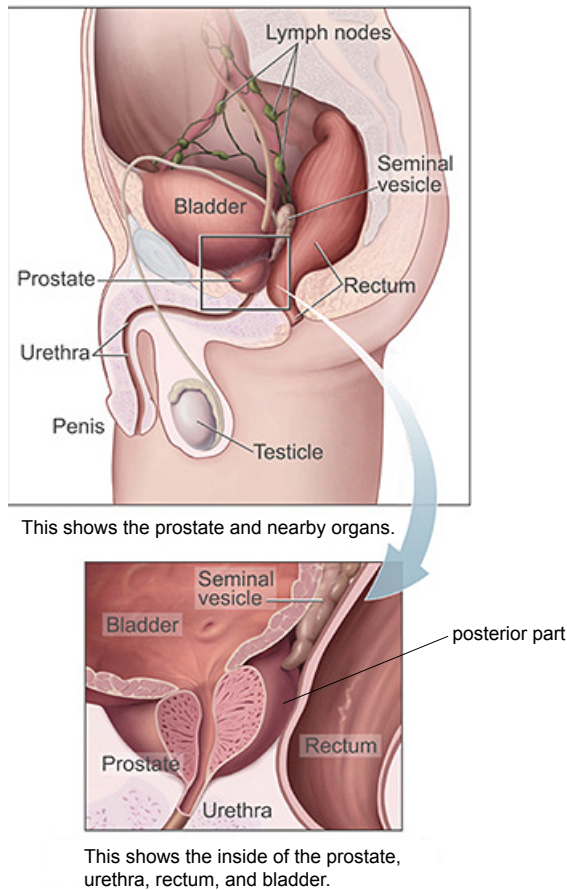
Figure 4.1: The prostate anatomy.[1]

❐ It contains citric acid used by sperm to mobilize energy via ATP (adenosine triphos-
phate) production.

❐ It contains an antibiotic, seminalplasmin, which may help to reduce the bacterial
content in the semen and in the female reproductive tract.

4.2.2   The porcine prostate

The male reproductive system of the pig is composed of the same structures as in
humans [38]. In contrast to the human prostate, the porcine prostate consists of two

---

[1]Modified from Wikipedia, `http://en.wikipedia.org/wiki/Prostate`, May 2011.

parts, compacta and disseminata [39]. The compact part appears as a number of rounded elevations on the dorsal (towards the back) side of the urethra, whereas the disseminate part surrounds the urethra [39, 40]. The two parts are histologically similar [39]. Prostate stones are present only occasionally in the boar prostate [39]. Nicaise et al. [40] used light and electron microscopy to study the disseminate prostate of 12 boars and 8 barrows, i.e. castrated boars. The prostate of the barrows did not develop normally. The authors concluded that the results permitted the use of the boar prostate as an experimental model for studying the influence of hormones used in human medicine.

4.2.3 Prostate cancer

In Sweden about 10 000 men are diagnosed with PCa each year and more than 2500 die from the disease, making it the most common cause of cancer-related male death [1]. Scandinavia and the Baltic region (Estonia, Latvia and Lithuania) have the highest PCa mortality rates in Europe [41]. PCa is often without symptoms, even in men with aggressive tumors, until severe stages [42]. Estimations based on autopsies show that up to 50% of men harbor PCa by 70 years of age [42, 43]. However, the vast majority of tumors are indolent [8]. In its most aggressive form PCa disperses metastases and is very dangerous; the 5-year survival rate is only 34% [44]. In contrast, survival is 100% if the cancer has not spread beyond the structures adjacent to the prostate or metastasized to distant lymph nodes [44].

Almost all, 95%, of prostate tumors form in the prostatic ducts in the glandular epithelium [44]. The majority develop in the posterior part of the gland (the peripheral zone) [45, 46], which is situated towards the rectum (Figure 4.1). PCa is usually multifocal and provides little contrast to healthy tissue using standard clinical imaging methods, such as ultrasound and MRI. This makes the cancer nodules difficult to detect [47, 48].

The causes of PCa remain largely unexplained [41]. Age, ethnicity and family history have been established as risk factors, and diet and genetic susceptibility may contribute [41].

4.2.4 Detection and diagnosis of prostate cancer

The clinical tests that are used for detection and diagnosis of PCa are the PSA test and SB. Historically, digital rectal examination, i.e. the physician palpates the prostate via the rectum, was the most important test [49, 50]. This method has low accuracy [48] and can usually only detect severe forms of PCa [50]. It is still used as a complement [50]. A high concentration of PSA in the blood indicates cancer [51]. However, the PSA level can be elevated also for men without PCa, often due to BPH [51], and men with normal levels may still have cancer [52]. A multicenter European randomized study including 182 000 men found that PSA-based screening reduced the PCa mortality by 20% [8]. However, it also caused unneccessary treatments and overdiagnosis, i.e. confirming cancer in patients with indolent tumors that would never cause clinical symptoms in their lifetime. To prevent one death 1410 men would have to be screened and 48 additional patients would have to undergo treatment. A similar study in the US, which enrolled almost 77 000 men,

did not find any significant benefits of PSA screening [53]. One possible explanation for the different outcomes is that the European study used a PSA cutoff of $3\ \mathrm{ng\,mL^{-1}}$ in most centers, as compared to $4\ \mathrm{ng\,mL^{-1}}$ in the US study. In addition, about 50% of the patients in the control group in the US were screened as part of usual care [53]. It has been estimated that the rate of overdiagnosis due to PSA screening is 50% [54].

If PCa is suspected from elevated PSA or digital rectal examination SB is performed [50]. An ultrasound probe equipped with a spring-loaded biopsy gun is inserted into the rectum, and the biopsy needle is directed to at least six predetermined sites according to the SB protocol [50]. SB fails to detect 20–30% of present tumors [7]. This can be appreciated since the volume of a biopsy typically is less than one thousandth of the prostate volume [55].

The diagnosis of PCa is determined through histological analysis of tissue sections from the biopsy samples or from the removed prostate when surgery has been performed. Montironi et al. [56] give a detailed description of a recommended procedure for preparation of radical prostatectomy specimens. In brief, first the removed prostate is fixed by injection of formalin at multiple sites using a needle. The surface is inked, and the prostate is immersed into formalin for 24 hours. The prostate is then cut into 4-mm thick slices, which are embedded in paraffin. A microtome is used to cut a 5-μm thick specimen from each of the embedded slices. The specimens are stained with hematoxylin and eosin to induce contrast for histological examination. Under a light microscope a trained observer can recognize different tissue types and distinguish healthy and cancerous tissue (Figure 4.2). The aggressiveness of detected tumors can be assessed from the histological appearance of the prostatic glands following the Gleason grading system [55]. This method is subjective, and the rates of intra- and interobserver disagreement are high [55]. The severity of PCa is clinically rated using a standardized system that defines different stages due to Gleason score and the spread of the primary tumor and metastases [44]. Today the patients diagnosed with PCa have tumors of lower grade and lower stage than 20 years ago, but there is still a wide range of aggressiveness [7]. Most patients have tumors of medium Gleason score, and due to the deficiencies in the practice of the Gleason system predictions of disease progression are often uncertain [55]. The physicians are then faced with a weak foundation for choosing an appropriate treatment.

The main imaging methods for detection of PCa are transrectal ultrasound and MRI. Due to a number of limitations, these techniques are not yet routinely used clinically for direct PCa detection [7,57]. New advances are very promising, but further clinical trials are needed [57,58].

4.2.5   Treatments of prostate cancer

Radical prostatectomy is the recommended treatment for men with aggressive, localized (no metastases present) PCa [15]. It has excellent long-term PCa-specific survival rates [59]. Unfortunately, serious side effects are common. Coelho et al. [60] estimated that $> 40\%$ of the patients were impotent and about 20% were incontinent 12 months after surgery. Today a rapidly increasing amount of radical prostatectomy procedures are performed using robotic assistance, which shows promise for improving surgical quality and decreasing
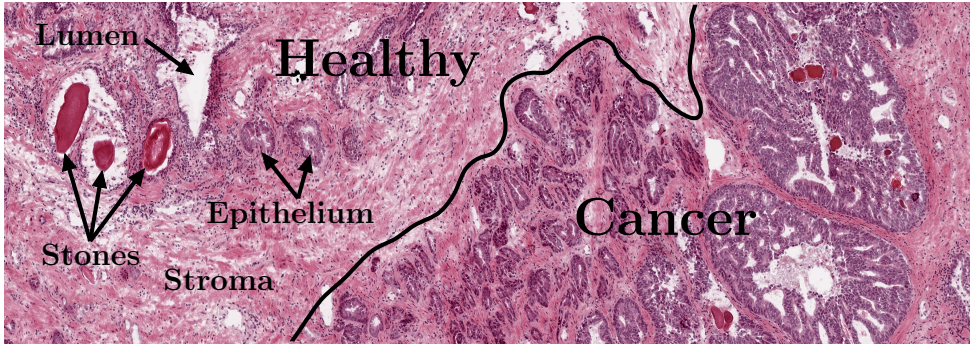
Figure 4.2: A scan (ScanScope CS, 20× objective, Aperio, Vista, CA, USA) of a histology specimen from the prostate of a 67-year old man who was diagnosed with PCa and underwent radical prostatectomy. The dimensions of the scanned area are 4 × 1.4 mm. The black line indicates the border between healthy and cancerous tissue.

side effects [60, 61].

After surgery the PSA level is monitored to assess the effectiveness of the treatment. For approximately 35% of patients, PSA will be detectable within ten years after surgery, which indicates clinically significant cancer recurrence [62, 63]. The risk is increased for aggressive cancers and if positive surgical margins are present [16]. Whether patients with aggressive, localized tumors who underwent radical prostatectomy would benefit from additional treatment using radiotherapy, chemotherapy, hormonal therapy or combinations of these is controversial [15, 64]. About 50% of those patients are cured with surgery alone, and they are then spared the side effects and toxicity of additional therapy [15]. Interestingly, van der Kwast et al. [62] found that adjuvant radiotherapy was significantly beneficial only for patients with positive surgical margins. The study included 1005 men. Thus, to reduce the rate of cancer recurrence while minimizing the use of unnecessary adjuvant therapy a method for intraoperative analysis of the surgical margins is greatly needed.

4.3   Tactile resonance method

4.3.1   The piezoelectric effect

The piezoelectric effect was discovered by the brothers Pierre and Jacques Curie in 1880 [65]. They demonstrated that when pressure was applied to a crystal, such as quartz or topaz, an electric potential was generated. The inverse effect also applies, a piezoelectric element changes shape if exposed to an electric field, and will therefore oscillate in response to a sinusoidal voltage variation. A piezoelectric element works as a transducer between electric and kinetic energy. The phenomenon originates from the fact that the unit cells of a piezoelectric material behave like electric dipoles, i.e. a non-uniform

charge distribution arises because the elementary cells have no center of symmetry. If pressure is exerted on the material the shape of the dipoles is altered, and this will induce a net electric potential in the material. Resonance sensors are typically made from a ceramic piezoelectric material, e.g. lead zirconate titanate (PZT), which can be pictured as a mass of tiny crystals, so-called crystallites, exhibiting dipole characteristics. The unit cells of the crystallites are non-centrosymmetric below the Curie temperature (the critical point below which the material is ferromagnetic), which usually is of the order of 1000 K ($\sim 700\,°C$) [66]. A ceramic can be given its piezoelectric properties by heating it to just below the Curie temperature and applying a strong electric field over it. The ceramic is then polarized in the direction of the applied field, and the dipoles are locked when the field is withdrawn.

4.3.2   Principle of the tactile resonance method

The principle of the TRM was presented by Omata & Terunuma in 1992 [67]. It is based on a piezoelectric PZT transducer divided into two parts, a driving element that generates vibration, and a pick-up element that detects the frequency of vibration. The transducer is set into oscillation by an electronic feedback circuit consisting of an amplifier, a bandpass filter and a phase-shift circuit, as shown in Figure 4.3 [67]. The signal from the pick-up is fed back to the circuit. The phase-frequency characteristics of the PZT transducer and the electronic circuit determine the oscillation frequency of the whole system. The phase-shift circuit establishes resonance at a user-selected frequency by ensuring that the sum of the phase shifts in the system is zero. To obtain a high sensitivity it is advantageous to choose a frequency close to the inherent resonance frequency of the PZT element. A probe tip is glued to the end of the PZT element (Figure 4.3). It is made in a shape and from a material suitable for the measurement task at hand. As the tip comes into contact with an object the resonance frequency changes, and the shift is related to the stiffness of the material [67]. The absolute frequency shift increases with the stiffness of the probed material. For relatively soft objects, such as silicone gum and the palm of a hand, the shift is negative, whereas it is positive for hard materials such as teeth and glass [67]. Murayama & Omata [68] developed an MTS by using a tip in the form of a 30 mm long, tapered glass needle with a very small spherical tip, from 1 mm down to 0.1 μm in diameter.

4.3.3   Theory

Kleesattel & Gladwell introduced a surface hardness tester called the contact-impedance meter in two publications in 1968 [69, 70]. Their theoretical explanations could later be applied to describe the characteristics of the TRM [67, 71]. A piezoelectric tactile resonance sensor can be modeled as a finite rod vibrating at its resonance frequency in the direction of its length [67, 69–71]. The probe tip is assumed to be hemispherical. The frequency change as the sensor comes in contact with an object can be expressed as

$$\Delta f = -\frac{V_0 \beta_x}{2\pi l Z_0} \tag{4.1}$$
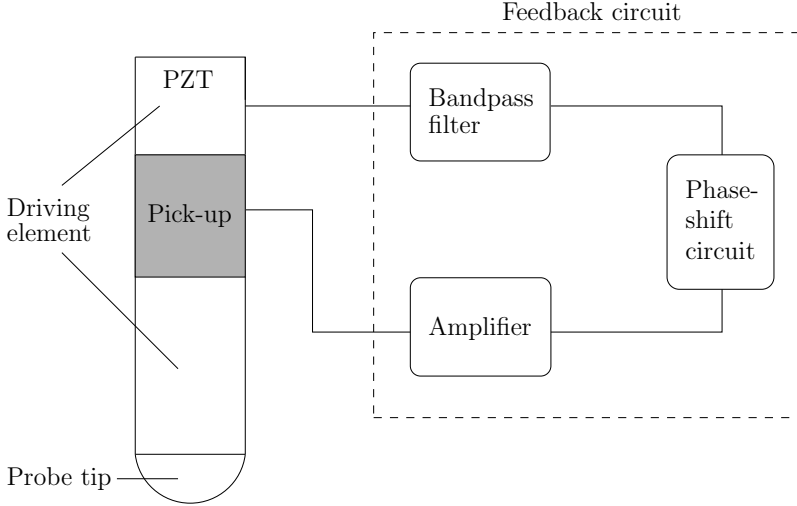
Figure 4.3: The principle of the TRM.

where V_0 is the wave velocity in the rod, l is the length of the rod, Z_0 is the acoustic impedance of the rod and β_x is the reactance part of the acoustic impedance

$$Z_x = \alpha_x + i\beta_x \tag{4.2}$$

of the probed object, where α_x is the resistance. β_x can be written as

$$\beta_x = m_x\omega - \frac{k_x}{\omega} \tag{4.3}$$

where ω is the angular frequency, m_x is the contact mass and k_x is the contact stiffness. m_x and k_x depend on the surface contact area S and can be written as

$$m_x = \frac{4a_{11}}{\pi^{3/2}(1-\nu)}\rho S^{3/2} \tag{4.4}$$

$$k_x = \frac{2E}{\pi^{1/2}(1-\nu^2)}S^{1/2} \tag{4.5}$$

ν is Poisson's ratio, ρ is the density, E is the elastic modulus (Young's modulus), and a_{11} is a coefficient that depends on ν [70]. $S = \pi r^2$, where r is the radius of the contact area. From (4.3)–(4.5) we see that for large contact areas m_x will dominate, whereas k_x will dominate for small contact areas [67]. Furthermore, at high frequencies the contribution from $m_x\omega$ increases, whereas k_x/ω becomes more important at low frequencies.

Jalkanen et al. [71] examined the theoretical model of the finite rod for theVenustron® system. The resonance frequency was 58 kHz and the probe had a hemispherically shaped

tip with 5 mm diameter. They showed that, since $m_x\omega \gg k_x/\omega$ for that system, the surface stiffness term k_x/ω in (4.3) can be neglected. (4.1)–(4.4) then give

$$\Delta f \propto \rho S^{3/2} \tag{4.6}$$

for a specific rod vibrating at a constant frequency, if Poisson's ratio is assumed to be constant [71]. The surface contact area S depends on the contact force between the sensor tip and the measurement object, F, according to $F \propto E S^{3/2}$ [71]. Substituting this relationship into (4.6) results in

$$\Delta f \propto \frac{\rho F}{E} \tag{4.7}$$

A stiffness sensitive parameter $\partial F/\partial \Delta f$ can then be derived as

$$\frac{\partial F}{\partial \Delta f} \propto \frac{E}{\rho} \tag{4.8}$$

Jalkanen et al. [71] experimentally verified this theoretical model in measurements on human prostate tissue. Their study showed that density variations were small and mostly non-significant, validating the use of $\partial F/\partial \Delta f$ as a stiffness sensitive parameter.

For the MTS the contact area is small and the inertia term $m_x\omega$ will be smaller than the surface stiffness term k_x/ω and can usually be neglected [72]. (4.1) can then be written as

$$\Delta f = \frac{V_0 k_x}{2\pi l Z_0 \omega} \tag{4.9}$$

According to Murayama & Omata [68] Hertz theory can be applied for small indentation depths δ, and the contact area S can then be modeled as a function of δ. They showed that from (4.5) and (4.9) a stiffness sensitive parameter can be obtained as $\Delta f/\delta$, which is related to Young's modulus [68]. They calculated Young's modulus from the slope of the frequency versus indentation curve, and verified that $\Delta f/\delta$ correlated highly with E in experiments on silicone samples.

4.3.4   Sensing volume

Jalkanen et al. [21] investigated the sensing volume of the Venustron® TRM system. They concluded that the tip laterally sensed a larger area than the actual contact area and had an estimated penetration depth of 3.5–5.5 mm for an indentation depth $\delta = 1$ mm. There was an approximate linear relationship between the indentation depth and the sensing depth; the sensor probed deeper into the tissue at larger indentation depths. For $\delta = 2$ mm the penetration depth was estimated to be up to 10 mm. Using an array with 64 TRM sensor elements Murayama et al. [73] demonstrated that tumors in the breast larger than 10 mm could be detected at depths up to 20 mm. TRM has higher potential for noninvasive detection of PCa than RS.

4.3.5 Detection of prostate cancer

Eklund et al. [37] were the first group to measure the stiffness of human prostate tissue using TRM in vitro. A catheter type sensor was used. The catheter was 2 mm in diameter. A hemispherical tip was formed from epoxy and attached to the PZT element, sealing the end of the catheter. They used a proposed model where the tissue stiffness was linearly related to the amounts of glandular tissue and prostate stones. A correlation of $R = -0.96$ between the measured and the expected stiffness was found. The tissue was fixed in formalin, which in general hardens the tissue. The results indicated that stroma and prostate stones were relatively hard tissue components, while glandular tissue was softer. Jalkanen et al. [19, 20] examined fresh human prostate tissue with the Venustron® system. A slice of prostate was measured directly after surgical removal. The authors showed that TRM could distinguish glandular tissue from cancerous tissue. In the first study [20] ten samples from ten patients were tested. A p-value < 0.001 was obtained for a MANOVA test of the difference between cancerous ($n = 13$) and healthy ($n = 98$) tissue. Only measurement sites consisting of 100% cancerous tissue were significantly stiffer than the glandular tissue. Stroma and sites with an accumulation of prostate stones could not be differentiated from cancer in those studies. However, PCa usually develops in the posterior part of the prostate [45, 46], where glandular tissue is abundant [19]. Thus, a stiff nodule in this area could indicate cancer [19]. In a recent study [74] Jalkanen demonstrated that hand-held measurements using the Venustron® could accurately determine the stiffness of gelatin ($R^2 = 0.94$). For hand-held measurements the impression speed is unknown, but Jalkanen showed theoretically and experimentally that this factor is not significantly related to the measured stiffness, which is promising for in vivo measurements. Murayama et al. [75] used an elasticity mapping system with an MTS to scan 300 μm-thick prostate sections from two patients. The tip of the MTS was 10 μm in diameter, and the scanning step-size was 5 μm. They found that the proportion of stiff points was larger for cancerous tissue. However, the stiffness distribution of healthy and cancerous tissue overlapped. No statistic evelution was performed.

4.4 Raman spectroscopy

4.4.1 The Raman effect

When a laser beam illuminates a tissue sample most photons are elastically scattered, i.e. their energy is conserved. A fraction of the photons are inelastically scattered and loose or gain energy as they interact with the biological molecules. There are three main inelastic scattering events: fluorescence, phosphorescence and Raman. Fluorescence and phosphorescence are associated with electronic transitions of the participating molecules. Raman scattering is a relatively weak process (quantum yield 10^{-8}–10^{-6}) in which incident photons set molecular bonds into vibration [76]. The energy of the scattered photons is shifted corresponding to the difference between the initial and final vibrational energy levels. A Raman spectrum is a plot of the scattered intensity versus the energy shifts.

Since every molecule has a unique set of bond vibrations, the spectrum is like a fingerprint of the sample. By convention the energy shift is expressed as a wavenumber shift termed Stokes shift and measured in cm^{-1} (the number of wavelengths per cm) [77]:

$$\Delta \tilde{\nu} = \frac{1}{\lambda_i} - \frac{1}{\lambda_e} \tag{4.10}$$

where λ_i and λ_e are the wavelengths of the incident and emitted photons, respectively.

The Raman effect was predicted by quantum mechanics in publications by Smekal in 1923 and Kramers & Heisenberg in 1925 [78]. It was experimentally verified in 1928 by the Indian professor Sir C. V. Raman. He observed the phenomenon in a delicate experiment using filtered sunlight as excitation source, a telescope to collect the scattered light and the eye as detector [79]. He was awarded the Nobel prize for the discovery already two years later.

Classical physics explains the basic principles of Raman scattering [76, 80]. As a molecule is hit by a photon its electron cloud is distorted by the electromagnetic field. The geometry of the cloud is changed and the molecule is excited to a virtual, higher state of energy. This state is unstable; the nuclei of the molecule cannot establish new equilibrium positions in response to the rearrangement of electrons. As the molecule relaxes the nuclei are set into vibration and a photon is emitted. The process is fast (10^{-13}–10^{-11} s) compared to fluorescence (10^{-9}–10^{-7} s) [81]. Consider a diatomic molecule irradiated by monochromatic light with frequency ν_0. The electrical field $E = E_0 \cos (2\pi\nu_0 t)$, where t denotes time, induces a dipole moment

$$P = \alpha E = \alpha E_0 \cos (2\pi\nu_0 t) \tag{4.11}$$

in the molecule. The polarizability α is a function of the nuclear displacement, because as the molecule changes shape, size or orientation the electron cloud can become easier or more difficult to distort. If the nuclei vibrate with a frequency ν_m, the nuclear displacement q can be expressed as $q = q_0 \cos (2\pi\nu_m t)$, where q_0 is the amplitude of the oscillation. Since $\alpha(q)$ can be regarded as a linear function of q for small amplitudes of vibration, it can be expanded as

$$\alpha = \alpha_0 + \left(\frac{\partial \alpha}{\partial q}\right)_0 q + \ldots \tag{4.12}$$

where α_0 is the polarizability at $q = 0$. Substituting (4.12) into (4.11), and using the formula $\cos \gamma \cos \beta = \frac{1}{2} \cos (\gamma - \beta) + \frac{1}{2} \cos (\gamma + \beta)$, we obtain

$$P = \underbrace{\alpha_0 E_0 \cos (2\pi\nu_0 t)}_{\text{elastic}} + \frac{1}{2} \left(\frac{\partial \alpha}{\partial q}\right)_0 q_0 E_0 \left[\underbrace{\cos (2\pi(\nu_0 - \nu_m)t)}_{\text{Stokes}} + \underbrace{\cos (2\pi(\nu_0 + \nu_m)t)}_{\text{anti-Stokes}}\right] \tag{4.13}$$

The three terms in (4.13) symbolize dipoles that oscillate with frequencies ν_0, $\nu_0 - \nu_m$ and $\nu_0 + \nu_m$. They describe elastic, Stokes and anti-Stokes scattering, respectively. In anti-Stokes scattering the photons gain energy. This is possible only when the molecule
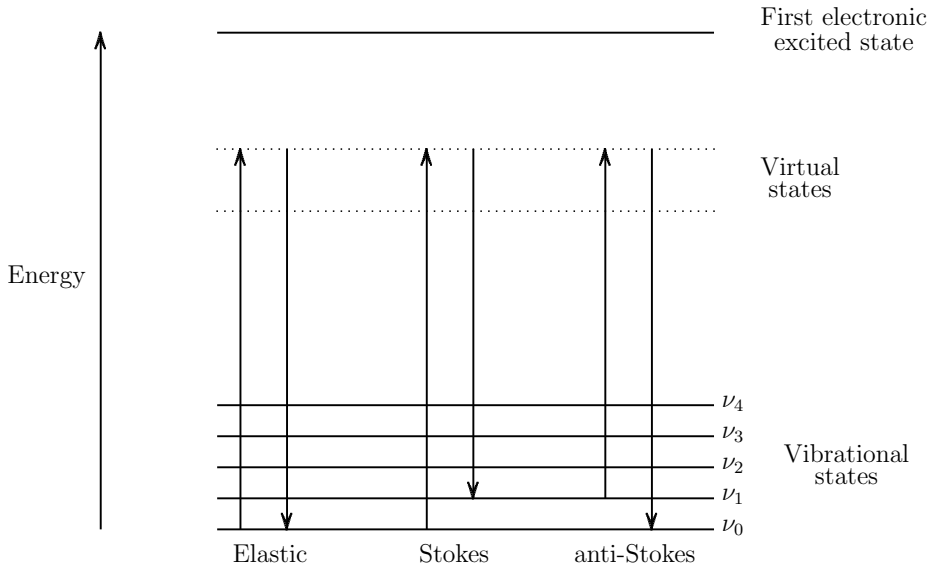
Figure 4.4: Energy diagram of elastic and Raman scattering. Incident photons are shown as upward arrows and emitted photons as downward arrows.

initially is at a higher vibrational energy level (Figure 4.4). At room temperature higher levels are sparsely populated and anti-Stokes scattering is weak. A fundamental property of the Raman effect is understood from (4.13): if $\left(\frac{\partial \alpha}{\partial q}\right)_0 = 0$, no Raman scattering will occur. This means that a specific molecular vibration is Raman active only if the polarizability is changed during the vibrational cycle. Symmetric vibrations usually cause the largest polarizability changes and generate the strongest scattering [76]. In general the scattering intensity I depends on the laser power l_p, the frequency of the laser light, ν_0, and the polarizability α, according to [76]:

$$I \propto l_p \alpha^2 \nu_0^4 \tag{4.14}$$

Hence, the Raman intensity is much stronger if a laser with short wavelength is used.

Quantum physics can be applied to calculate the frequencies of the molecular vibrations [80]. As an example, consider the vibration of a diatomic molecule. It can be modeled as a harmonic oscillator for a single particle. The chemical bonding between the nuclei is pictured as a Hookian spring with a force constant k, and the potential energy $V(q) = \frac{1}{2}kq^2$, where q is the displacement. The Schrödinger equation for this model becomes

$$-\frac{h^2}{8\pi^2 m}\frac{\partial^2 \Psi}{\partial q^2} + \frac{1}{2}kq^2\Psi = E\Psi \tag{4.15}$$

h is Planck's constant, m is the mass of the particle, Ψ is the wave function and E is the total energy of the particle. The solutions are eigenfunctions with the corresponding

eigenvalues

$$E_v = hc\tilde{\nu}\left(v + \frac{1}{2}\right) \tag{4.16}$$

c is the speed of light, $v = 0, 1, 2, \dots$ is the vibrational quantum number, and

$$\tilde{\nu} = \frac{1}{2\pi c}\sqrt{\frac{k}{m}} \tag{4.17}$$

is the wavenumber [cm^{-1}] of the vibration. Hence, the rule of thumb is that strong bonds and light atoms will give rise to high vibrational frequencies and vice versa [76]. From (4.16) we see that the energy is quantized with a constant separation between energy levels equal to $hc\tilde{\nu}$. This is a good approximation for lower energy levels, but for actual molecules the separation decreases av ν increases [80]. The selection rules of quantum mechanics prohibit many vibrational transitions [80]. For the harmonic oscillator, only transitions that fulfill $\Delta v = \pm 1$ are allowed. The transition $v = 0 \leftrightarrow 1$ normally produces the most intense peak in the Raman spectrum, since most molecules are in their lowest state of energy E_0 at room temperature. For polyatomic molecules the vibrational patterns can be very complicated. However, in principle the complicated vibrations can be described as a superposition of harmonic oscillations for all nuclei [80].

4.4.2 Instrumentation

A Raman spectrometer basically consists of a laser generating monochromatic light, a sample illumination and collection system, a filter that separates the elastically- and the inelastically-scattered light, a wavelength selector (e.g. a grating) and a detector [80]. Modern systems for tissue measurements typically use NIR diode lasers and CCD detectors [82]. Microscopes or fiber optic probes in the backscattering collection geometry are commonly used to illuminate the sample and collect the Raman light [30]. Figure 4.5 shows a schematic drawing of an RS fiber optic setup.

The development of RS fiber optic probes enables in vivo measurements. Several factors complicate the realization of fiber optic probes. Fused silica fibers generate a strong signal in the Fingerprint spectral interval, which necessitates the use of extra filters at the probe tip to block this radiation [28]. For clinical use the probes need to be flexible and thin, of the order of 1–2 mm to be incorporated into biopsy needles, endoscopes and other devices [83]. They must withstand clinical sterilization routines [83]. Several different probes have been developed, but so far the manufacturing process has been complicated and expensive [28]. However, several technical advancements in the construction of fiber optic probes have been presented recently [28, 84, 85]. Furthermore, RS measurements in the high wavenumber region, from 2400 to 3800 cm^{-1}, can be performed using simpler probes without filters, since little Raman signal is generated in the probe itself in this region [86–88].

Komachi et al. [89–92] have developed a 0.6 mm thin probe, and demonstrated promising results in measurements of the esophagus and stomach of the living rat [92]. The probe consists of a central delivery fiber surrounded by eight collection fibers. They
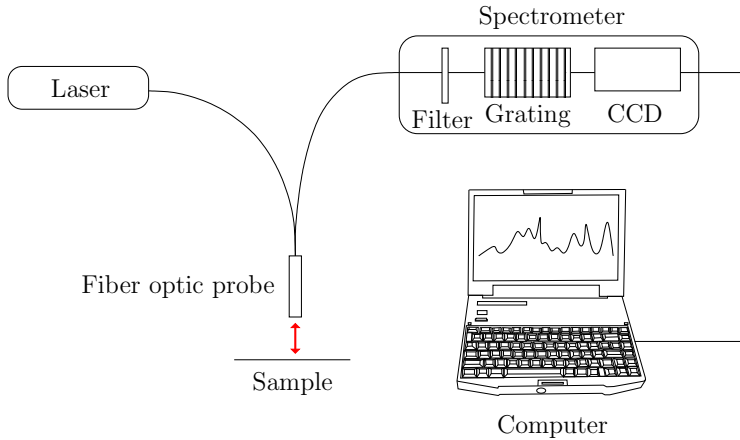
Figure 4.5: A typical RS fiber optic setup.

claim that it can be commercially manufactured at a low cost [89]. Day et al. [84] describe the development of a miniature, confocal fiber optic probe. Their aim was to construct a probe capable of sampling tissue layers 100–200 μm below the tissue surface, which would be optimal for early detection of esophageal cancer. The depth of field was 147 μm in measurements on polished silicon. In a recent publication the group attained 66–81% sensitivity and 80–98% specificity for discriminating esophageal cancer from healthy tissue using that confocal probe with an integration time of 2 s [85]. They measured 123 biopsy samples from 49 patients. The accuracy was increased for an integration time of 10 s.

The penetration depth in tissue of RS fiber optic probes using the backscattering collection mode is typically only several hundred micrometers [30]. Hence, deep-sited organs, such as the prostate, are inaccessible for noninvasive examinations. Development of RS techniques that can probe deeper into the tissue, such as time-gated RS, transmission RS, and spatially offset probes, is ongoing [30]. Spatially offset probes increase the accessible depth to several mm [30]. However, the spatial separation between excitation fibers and collection fibers makes the probes bulkier than ordinary probes. Using transmission RS identification of calcified materials buried at depths up to 2.7 cm in a breast cancer phantom have been demonstrated [93]. However, in transmission RS the sample is illuminated from one side and the Raman signal is collected from the opposite side; this approach may be difficult to use in vivo.

4.4.3 Raman measurements of tissue

RS is excellent for measuring the biochemical content of tissue for a number of reasons including:

❏ The majority of biological molecules are Raman active [81].

❒ Minimal or no sample preparation is required.

❒ Water is a poor Raman scatterer; it interferes little with the spectra of tissue [76].

❒ RS is sensitive to many factors that affect biomolecules, such as pH, degree of hydration, bacterial attack, etc. [94].

❒ The relative abundance of tissue components is proportional to their contributions to the Raman spectrum [83].

❒ In vivo measurements are feasible via fiber optic probes.

Some of the drawbacks with the method are:

❒ Tissue autofluorescence can distort the Raman signal.

❒ Acquisition of high quality spectra often requires long integration times. Therefore, in vivo measurements may be affected by motion artifacts.

❒ The instrumentation is sensitive to surrounding light.

❒ Current fiber optic probes have a short penetration depth in tissue [30].

RS measurements of tissue were long hampered by the strong, broadband tissue autofluorescence induced by lasers in the visible region [83]. Modern NIR RS systems have largely overcome this problem, since NIR light has too low energy to initiate most fluorescence processes [83]. Autofluorescence of tissue is believed to be generated mainly by a few fluorophores such as flavins, nicotinamide adenine dinucleotide, aromatic acids such as tryptophan, tyrosine and phenylalanine, and porphyrins [95]. Several different approaches for minimizing fluorescence interference have been demonstrated. Time-gating and wavelength shifting can effectively decrease fluorescence, but these require modifications of the Raman instrumentation [96]. An alternative is to use mathematical methods to subtract the fluorescence signal. However, many algorithms cause spectral artifacts [96]. Polynomial fitting does not distort the Raman peaks to a high degree [96]. Lieber et al. [96] presented an algorithm that automatically subtracts the spectral background by fitting a modified polynomial to the spectrum. This method was further developed by Cao et al. [97].

The origin of many observed peaks in tissue spectra can often be interpreted with help of databases and published spectra of biological molecules [81, 98]. Tissue generally produces spectra with relatively narrow bands, typically 10–20 cm^{-1} wide [83]. Stokes shifts from 200–3600 cm^{-1} usually cover the information of interest [76]. The characteristic vibrations of the most common chemical groups have been assigned approximate wavenumber ranges that are valid for the groups in most structures [76]. The spectral region 4000–2500 cm^{-1} is where single bonds (X−H) scatter, the interval 2500–2000 cm^{-1} is where multiple bonds (−N=C=O) occur, and the range 2000–1500 cm^{-1} includes double bonds (−C=O, −C=N, −C=C−). The interval 1900–700 cm^{-1} is referred to as the Fingerprint region. Many molecules exhibit complex vibrational patterns that yield unique spectral features in this region, which is densely packed with sharp bands [81]. Raman peaks below
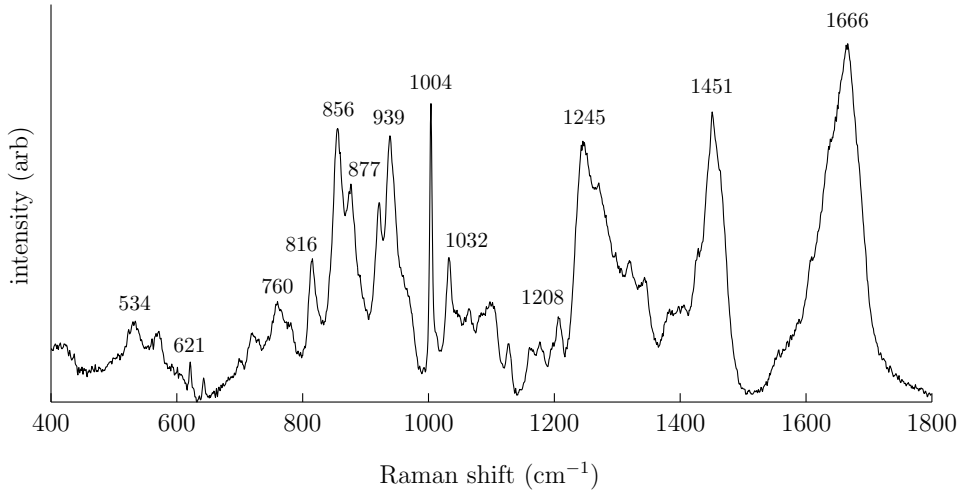
Figure 4.6: A spectrum of porcine prostate tissue recorded in our laboratory using a Raman micro spectrometer (Renishaw system 2000, Renishaw, Wotton-under-Edge, UK). The integration time was five minutes.

650 cm^{-1} normally belong to inorganic groups, metal-organic groups or lattice vibrations. RS can explore the primary, secondary, tertiary and quaternary structure of biological molecules [81]. For example protein structure, DNA conformation and cell membrane conformation can be probed. Databases over characteristic peak frequencies of important biological molecules are available, see e.g. Movasaghi et al. [98]. Figure 4.6 shows an example of a porcine prostate spectrum. Tentative assignments of the major peaks identified in the spectrum are given in Table 4.1.

There is an abundance of diagnostic features for cancer detection in the spectra of various tissues [81]. The ratio of intensities of the amide I vibrational mode at 1655 cm^{-1} to the CH$_2$ bending vibrational mode at 1450 cm^{-1} can be used to differentiate healthy and cancerous tissue in brain, breast and gynecological tissues. Cancer induces a significant increase of the DNA content [27,81,99]. The amide III band at 1260 cm^{-1} may contribute towards cancer identification, e.g. the amide III band is broadened in cancerous gynecologic tissue.

Several in vitro studies [24–27, 29, 99, 101] have investigated the potential of RS to detect and grade PCa. Crow et al. [25] attained 98% sensitivity and 99% specificity for differentiating four cell lines with varying degrees of aggressiveness. Cells were placed onto a calcium fluoride slide, and about 50 spectra from each cell line were measured. A total of 200 spectra were input to the diagnostic algorithm, which used principal component analysis (PCA) and linear discriminant analysis. Taleb et al. [99] attained a 100% accurate classification of healthy and cancerous (derived from metastases) prostate cells ($n = 30$). They concluded that the most significant spectral change due to cancer

Table 4.1: Tentative assignments [98–100] of the major peaks in the porcine prostate spectrum shown in Figure 4.6.

Peak position (cm^{-1})	Assignments
1666	Amide I (proteins)/C=C lipid stretch
1451	CH_2 bending mode of proteins and lipids
1245	Amide III (proteins, 1240–1265 cm^{-1})
1208	Tryptophan and phenylalanine $\nu(C-C_6H_5)$ mode
1032	C−H in-plane bending mode of phenylalanine
1004	Symmetric ring breathing mode of phenylalanine
939	C−C stretching of collagen backbone
877	C−C stretching (collagen)/C−C−N$^+$ stretching (lipids)
856	Ring breathing mode of tyrosine/C−C stretch of proline ring
816	C−C stretching (collagen)/proline, tyrosine, ν_2 PO$_2^-$ stretch of nucleic acids
760	Symmetric breathing of tryptophan
621	C−C twisting mode of phenylalanine
534	S−S disulfide stretch in proteins

was an increase in the DNA content and a change in DNA conformation from B-DNA to A-DNA. Crow et al. [24] showed that prostate biopsy samples of BPH and cancer with different Gleason scores could be distinguished with an overall accuracy of 89%. They recorded 450 spectra from biopsies of 27 patients, 14 with BPH and 13 with PCa. Devpura et al. [29] identified $> 94\%$ of cancerous regions in RS measurements on 10 μm thick prostate specimens. They found that Gleason scores 6, 7 and 8 could be clearly separated. In the only publication using a fiber optic probe [26], PCa was distinguished from BPH and prostatitis with an overall accuracy of 86%. 38 prostate samples from 37 patients were measured. Stone et al. [27] estimated the gross biochemistry of BPH, prostatitis and PCa of different grades of aggressiveness (Gleason score < 7, $= 7$ and > 7). This was accomplished by comparing the spectra of the prostate samples to the spectra of pure chemical standards assumed to be the main tissue components. It was shown that the DNA content was increased in cancerous tissue. Furthermore, the cholesterol level increased substantially, the choline level was elevated but remained low, triolein was increased, while oleic acid decreased somewhat with progression of disease.

4.5   Tissue preparation and measurement procedures

In vitro experiments should be carefully designed so that the results and conclusions thereof are applicable to in vivo measurements. It is essential to avoid misinterpretation of results due to artifacts originating from tissue preparation and/or inappropriate measurement procedures.

Fresh tissue samples, immersed in physiological buffer to prevent tissue dehydration,

are ideal for in vitro RS studies [102, 103]. However, preservation of the samples is usually necessary since fresh samples are fragile, difficult to acquire and have a very limited shelf life [103]. Clinically, the most common method for archiving tissue samples is formalin-fixation and subsequent paraffin-embedding [104]. Unfortunately, paraffin-embedded samples are not suitable for RS measurements, since the paraffin generates a very strong signal that swamps the Raman signal from the tissue [104]. Deparaffinization of tissue is feasible, but biochemical information may be lost [104]. It is difficult to remove all paraffin, and the residuals cause interfering peaks in the spectra [104, 105]. Formalin fixation may be a suitable alternative preservation method [103, 104]. However, some studies have reported spectral artifacts in formalin-fixed tissue [102, 105].

Freezing of tissue is considered to be the best preservation method for RS studies [105]. Although it is one of the most commonly used methods [105], only a few studies have in fact confirmed its suitability [102, 105, 106]. Shim et al. [102] evaluated snap-freezing of ten different tissue types from hamster with a Fourier-transform Raman spectrometer, equipped with a 1064-nm laser. They compared fresh tissue to snap-frozen tissue stored at $-80\,°C$ for 1, 9 and 30 days. The frozen tissue was thawed immersed in phosphate buffered saline (PBS) at room temperature for 15 minutes. No spectral artifacts due to freezing or thawing were seen for the different tissue types, except for fat and liver. Their conclusion was that snap-freezing preserved the biochemical composition well. They pointed out that the results should be confirmed for other tissue types and species. To my knowledge no RS study of snap-freezing of prostate tissue has been presented in the literature before.

Raman spectrometers use relatively powerful lasers that may damage tissue, and the measured signal can then be distorted. Therefore, it is necessary to examine the effects of the laser illumination on the tissue. Modern RS systems adapted for tissue measurements use NIR lasers, which are less prone to harm the sample than lasers in the UV or visible region [107–109]. However, studies investigating effects from visible and NIR light irradiation of tissue at high intensity are rare. To my knowledge the effects of NIR laser illumination on prostate tissue have not been investigated using RS before.

The biomechanical properties of tissue may be different in vitro as compared to in vivo. It is well known that skeletal muscles stiffen significantly after death, so-called *rigor mortis*. However, less is known about how noncontractile soft tissues are affected [110]. Chan & Titze [110] studied the effects of postmortem changes and freezing-thawing of vocal fold tissues excised from dogs. They found no postmortem changes. Slow freezing in $-20\,°C$ caused a significant increase of stiffness, whereas no changes were observed when snap-freezing in liquid nitrogen was applied. They attributed the changes from slow freezing to the formation of large ice crystals, which disrupted the structure of the extracellular matrix. In another study on freezing of articular cartilage no stiffness changes were seen for either snap-freezing or slow freezing [111]. Freezing seems to be an appropriate preservation method for studies of tissue stiffness [112]. However, this has not been verified for prostate tissue.

For TRM measurements it is very important to prevent dehydration of the tissue, which will increase the stiffness [113]. Jalkanen et al. [19, 20] applied PBS regularly onto

the prostate slices during measurements using a brush. Murayama, Oie et al. [75, 114] used a moisture chamber at 36 °C for elasticity mapping with the MTS. The group later refined the experimental setup to let the tissue sample and the MTS be fully immersed in PBS [113, 115], which enabled measurements to be acquired for several hours without artifacts [115].

4.6   Mathematical tools for analysis and classification

Mathematical tools are essential for facilitating interpretation of complex multivariate data sets, such as the combined outputs from TRM and RS. Raman spectra of tissue contains a multitude of peaks (Figure 4.6), and they are difficult to interpret [98]. Multivariate methods such as PCA have become important for identifying the important spectral features for specific biomedical applications. Statistical analyses of data are necessary to support hypotheses about differences between various groups of tissue, e.g. between healthy and diseased tissue. Finally, characterization of tissue during medical examinations or surgery require efficient classification algorithms that provide relevant clinical information from a large set of variables in near real-time.

PCA is a valuable technique for data reduction and interpretation of data sets with a large number of variables [116]. It can often reveal connections not initially suspected. The principal components (PCs) are linear combinations of the original variables that account for a maximum amount of variability in the data. They are uncorrelated and each successive PC explains as much of the remaining variance as possible. Geometrically this represents a projection of the data onto a new coordinate system (Figure 4.7). The values for the observations in the new coordinate system are called PC scores. A few PCs can often describe a large amount of the total variability. Hence, a data set with n observations on p variables can be replaced by n observations on k PCs, where $k \ll p$, without much loss of information. The PCs are often used in subsequent analyses in place of the original data [116]. PCA is a valuable tool for spectroscopic applications [22]. For example, Taleb et al. [99] used PCA on RS data to study the differences between healthy and cancerous prostate cells.

Cluster analysis is an unsupervised technique for identifying natural groups containing similar observations [116]. No prior knowledge of the groups is needed; the algorithm defines the user-selected number of groups based on similarity measures, usually some sort of statistical distance between the observations. Hierarchical clustering analysis (HCA) starts out either by looking at all individual observations, or by considering the whole group, and then applies a number of successive merges or divisions. If we consider the former as an example, first all the distances between all observations are determined. Observations that are close together are grouped together. Next, these groups are merged to larger groups that are nearby, and so on and so forth. This continues until the predetermined number of groups have been defined [116]. Cluster analysis is useful for unsupervised differentiation of healthy tissue types, and for identification of diseased tissue, from spectroscopic measurements [22]. It has successfully been used to produce pseudo-color images of histology specimens from spectroscopic data that compare well
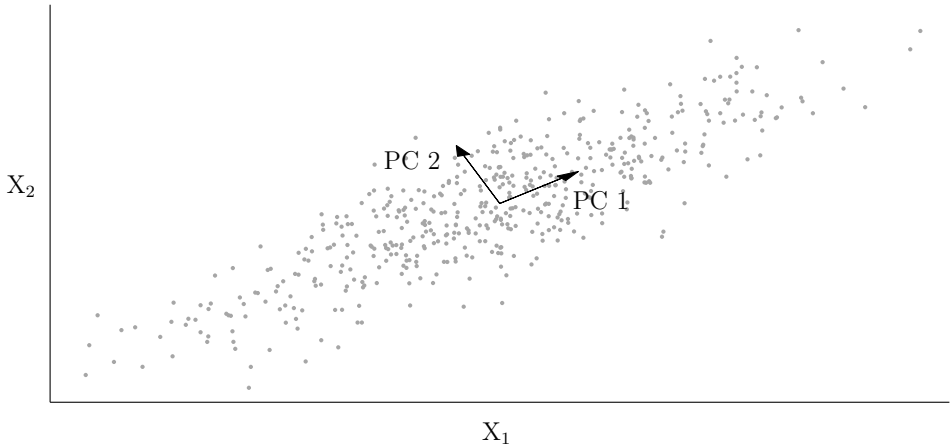
Figure 4.7: PCA on random data from a bivariate normal distribution. The PCs are vectors of unit length that point in directions of maximum variability. They will be the axes of the new coordinate system. For this example the first PC explains almost 95% of the total variability.

with standard histology images [22, 117].

The objective of data classification is to define a rule that can decide to which class a new observation belongs [116]. The rule is found by training the classifier to recognize patterns in data from observations of a relatively large number of samples of known classes. Classification techniques are supervised, in contrast to cluster analysis, where no classes are defined prior to analysis. Support vector machines (SVM) is a powerful classification technique that was introduced by Cortes & Vapnik in 1995 [118]. SVM calculates the hyperplane that separates two classes of data with the largest possible margin (Figure 4.8). Cortes & Vapnik introduced the concept of soft margins that enables classification of nonseparable data. The algorithm aims at minimizing the number of classification errors while separating the correctly classified observations with maximal margin [118]. To construct classification rules that generalize well, i.e. classify unseen data with low rate of error [118], cross-validation techniques can be used to find the optimal parameter settings for the SVM algorithm [119]. SVM can be used to separate more than two classes [120]. One strategy is to apply the binary classifier to distinguish two classes at a time, and determine the final class from the outcomes for all those classifications by a voting procedure [120]. SVM has attained very high classification accuracies in spectroscopic studies of cancerous tissues [121–123].
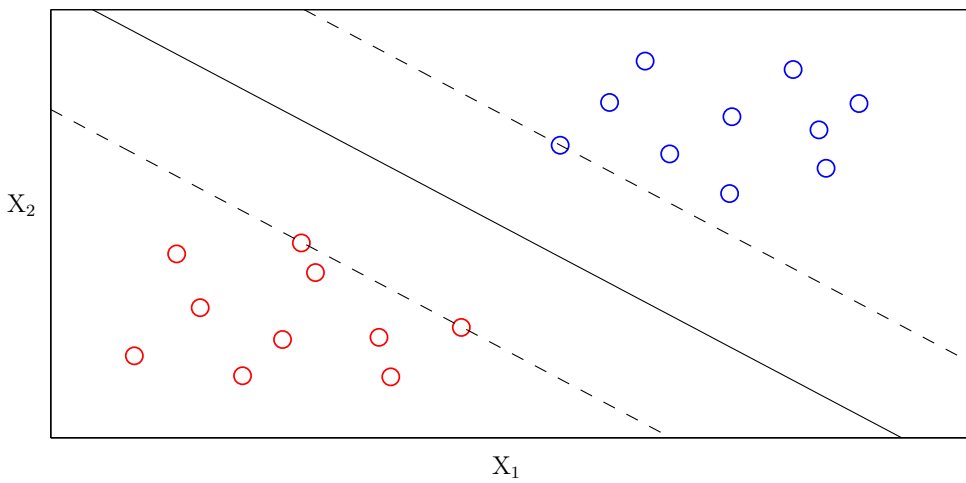
Figure 4.8: SVM classification of data from two groups, shown in red and blue, that are linearly separable. The solid line is the maximum-margin hyperplane, and the dashed lines show the margins. There are other planes that will separate the groups, but they will have smaller margins. The samples on the margins are called support vectors.

CHAPTER 5

Aims

The overall aim of this thesis was to explore the need for new, complementary methods for PCa detection and take the first step towards a novel approach: the combination of TRM and RS. The specific aims were:

❒ To review the different methods for localization and diagnosis of PCa, in order to explore the demand for new, complementary methods.

○ This objective was assessed in Paper A.

❒ To develop a robust procedure for RS measurements of tissue in vitro, and for mathematical preprocessing and multivariate analysis of RS data. In particular, to evaluate the effects of snap-freezing and NIR laser illumination on porcine prostate tissue using RS.

○ This objective was assessed in Papers B, C and D.

❒ To develop a multivariate approach for comparing TRM and RS information via measurements on porcine tissue in vitro, in order to investigate the correlation of the data and potential diagnostic power of the combination.

○ This objective was assessed in Paper C.

❒ To develop a novel setup combining a scanning haptic microscope employing an MTS and an RS fiber optic probe, and adapt the system for measurements of prostate tissue slices.

○ This objective was assessed in Paper D.

❒ To investigate the accuracy for classification of healthy porcine prostate tissue types, and healthy and cancerous human prostate tissue, using SVM classification of combined TRM and RS measurements with the above-mentioned system.

○ This objective was assessed in Paper D.

Material and Methods

This chapter summarizes the practical part of the work. It describes the equipment that was used, the measurement procedures and the data analysis. For more detailed information the reader is referred to Papers A–D.

6.1 Literature review

A review of the methods for localization and diagnosis of PCa was performed (A). The review focused on technical methods that can, or have the potential to, directly localize/diagnose PCa in situ via noninvasive or minimally invasive routes. Methods that label the tumor, e.g. with radioactive or fluorescent markers, were excluded. The databases Science Citation Index Expanded® and Social Sciences Citation Index® were searched via Web of Science®[1] for relevant papers using the following combinations of search words:

- ❒ prostate AND cancer AND imaging
- ❒ ultrasound AND prostate
- ❒ prostate AND spectroscopy NOT magnetic
- ❒ magnetic AND resonance AND prostate AND cancer
- ❒ Raman AND prostate
- ❒ resonance AND sensor AND prostate
- ❒ infrared AND spectroscopy AND prostate AND cancer
- ❒ prostate AND FTIR
- ❒ elastography AND prostate
- ❒ DWI AND prostate
- ❒ DCE MRI AND prostate

---

[1] `http://www.isiwebofknowledge.com`

All years of publication, 1975–2009, were included in the searches. Recent publications were favored. The reference lists in the selected articles were scrutinized for additional important papers. 185 publications were eventually selected for the review.

6.2   Experimental setup

Back in 2006 the research subject of Biomedical Engineering had just been established at the university. We did not have our own laboratory at that time. Therefore, a Raman micro spectrometer (Renishaw system 2000, Renishaw, Wotton-under-Edge, UK), which was available at the Dept. of Chemical Engineering and Geosciences, was adapted for measurements of tissue. This was done by installing a NIR laser with 830-nm wavelength (Renishaw HPNIR, 300 mW) and changing the filters of the setup. This system was used to study the effects of snap-freezing and NIR laser illumination on porcine prostate tissue (B). A water-dip objective (NIR Apo $60\times/1.0$W, Nikon, Tokyo, Japan) was used for spectral acquisition in the Fingerprint region, from 400 to 1800 cm^{-1}. The irradiance onto the samples was $\sim 3 \cdot 10^{10}$ W m^{-2}. To avoid interference from surrounding light the room was darkened during measurements. The spectrometer was calibrated for wavelength shift daily using the sharp silicon peak at 520 cm^{-1} as reference. The wavelength-dependent sensitivity of the CCD detector was calibrated using a tungsten halogen light source (LS-1-CAL, Ocean Optics, Dunedin, FL, USA).

A sophisticated laboratory for biomedical research was built up during 2006–2009. A state–of–the–art RS fiber optic system was purchased. It was composed of a 0.8 mm thin fiber optic probe (Machida Endoscope Co., Tokyo, Japan), of the same type used in [92], connected to a Raman spectroscope (RXN1, Kaiser Optical Systems, Ann Arbor, MI, USA). The spectroscope had a holographic grating that enabled simultaneous collection of the complete spectral interval from 100 to 3425 cm^{-1}. It incorporated a 400-mW laser at 785 nm (Invictus™, Kaiser Optical Systems). Proprietary software (iC Raman™, Kaiser Optical Systems) controlled the spectrometer. This setup was used for the RS measurements in Papers C and D. All RS measurements were performed in darkness, because spectral distortions from surrounding light were observed. The laser power was limited to avoid damage of the fiber optic probe due to heat building up at the tip. In Paper C it was set to 160 mW corresponding to approximately 80 mW onto the sample. For Paper D the probe was replaced with a more heat-resistant one, allowing use of higher power. The laser power was then set to 270 mW. This corresponded to an output effect at the probe tip of 140–150 mW. The integration time could be lowered from 30 s (C) to 7 s (D) without sacrificing spectral quality. The system was calibrated for wavelength shift and energy sensitivity once a month (HoloLab Calibration Accessory, Kaiser Optical Systems).

For performing the first combined TRM and RS measurements (C) the Venustron® (Axiom Co., Ltd., Kōriyama, Fukushima, Japan) TRM system was used in combination with the RS fiber optic setup. A customized setup was constructed (Figure 6.1). The RS fiber optic probe and the Venustron® sensor were mounted next to each other. A three-dimensional translation stage assured that measurements were performed at the
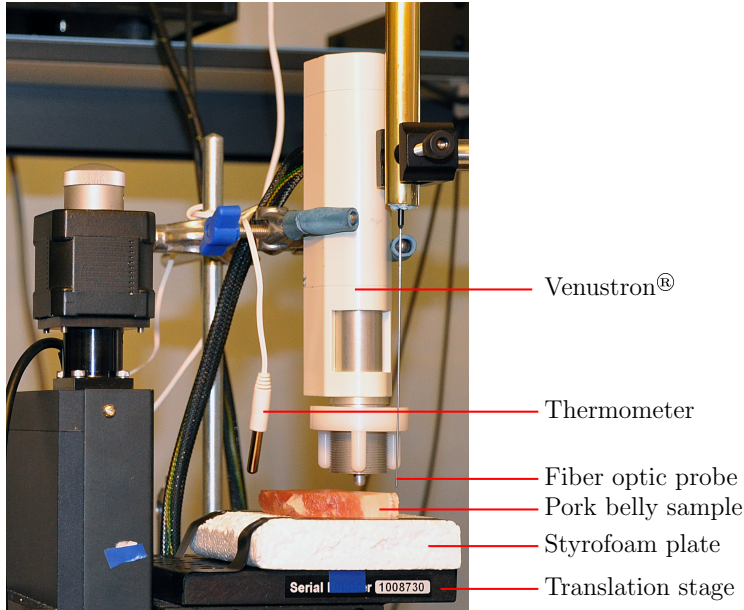
Figure 6.1: The experimental setup for Paper C.

same points with both probes. It was composed of three one-dimensional stages (NRT100, Thorlabs, Newton, NJ, USA) with a common control unit (BSC103, Thorlabs). To damp vibrations the whole setup was mounted on an optical table (PBG52513 – Metric UltraLight Series II breadboards, Thorlabs). The translation stage was controlled via a LABVIEW™ (version 7.0, National Instruments, Austin, TX, USA) program written in-house. A camera (Powershot S3 IS with close-up lens 500D and LAH-DC20 conversion lens adapter, Canon, Tokyo, Japan) was mounted above the setup. It was used to capture a picture of the tissue sample, which was loaded into the program. The user selected the measurement points from the picture. The coordinate system defined in the program was calibrated to have the origin at the top left corner of the picture. It was important to assure that the sensors measured on the same points of the sample. Their positions were calibrated by visually controlling that each sensor was positioned exactly above a reference mark when the translation stage was moved to the corresponding coordinates.

For Paper D a novel TRM technology was used, the MTS, which was developed by Murayama & Omata [68, 124, 125]. Their research group has developed an elasticity mapping system using the MTS, which has been termed scanning haptic microscopy (SHM) [115]. It has been commercialized, and we purchased such a prototype (P&M Co., Ltd., Aizuwakamatsu, Fukushima, Japan). A unique setup that combined the SHM system with the RS fiber optic setup was developed (Figure 6.2). It was composed of an XYZ-stage with a resolution of 0.01 μm and an actuator mounted on the Z-axis to

manipulate the MTS. The system incorporated a camera (LifeCam Cinema™, Microsoft, Redmond, WA, USA) and a USB microscope (Dino-Lite AM413TL, AnMo Electronics Corp., Hsinchu, Taiwan), to capture film and photos of the sample and probes. The temperature was logged by resistance measurement of a platinum resistance element (FK1020 PT1000, Heraeus, Kleinostheim, Germany) with a multimeter (Fluke 45, Fluke Corp., Everett, WA, USA), connected to the computer via GPIB. A labview™ program that controlled the hardware was developed. It automated the measurements as far as possible and collected all data except the RS data, which was recorded by the spectrometer software on a separate computer. The spectral acquisition could not be automatically triggered. Therefore, a photo diode was mounted close to the RS probe (Figure 6.2) to monitor when the laser was illuminating the sample. The shutter to the laser was closed by the spectrometer between the measurements. The spectrometer was set to continuous spectral acquisition, and the translation stage was moved to the next point as the photo diode voltage decreased abruptly. The voltage was measured with a second multimeter (Agilent 34401A, Agilent Technologies, Inc., Santa Clara, CA, USA) via the GPIB interface.

The SHM system was adapted for measurements of prostate tissue (D). The standard settings had to be adjusted and optimizations of the software were done. Since the prostate tissue was rather sticky the MTS was raised relatively far above the tissue after each measurement, approximately 100 μm, so that it detached from the tissue. The impression depth was set to about 40 μm, which made the mappings more stable for samples with uneven surfaces, as compared to the standard setting of $\approx$ 25 μm (half of the tip diameter). Each MTS had unique characteristics (Figure 6.3). The length and exact shape of the glass needle is very important for obtaining high sensitivity [125]. Some sensors were not suitable for prostate tissue measurements. One reason was that the stiffness range of the prostate tissue was wide, from 2 to 200 kHz, and some sensors did not give a linear response throughout this range. Another reason was that for some sensors the resonance frequency could change abruptly when very stiff points were measured. It was often challenging to identify a frequency where the sensitivity was high, the response linear, and the measurements were stable. The needles were fragile and easily broken due to operator mistakes. Several safety routines were implemented in the labview™ program to avoid this.

The positions of the MTS and the RS probe relative to the stage were determined by using a printed grid with 50 μm line thickness (D). A line intersection was used as reference mark. The MTS was aligned with the reference mark using the USB microscope. Since the RS probe was relatively large it was difficult to calibrate its position visually. Therefore, an RS mapping was performed. A cluster analysis was performed on the data using an HCA algorithm. The mesurement points were divided into three groups, and a mapping image was constructed. The line intersection was then clearly visualized (Figure 6.4), and the position of the RS probe was determined with high accuracy.

Z-actuator

Micro manipulator

Z-stage

USB microscope

Sample holder

XY-stage

Photo diode

PT 1000

MTS

PBS supply

Fiber optic probe

Camera

Glass needle
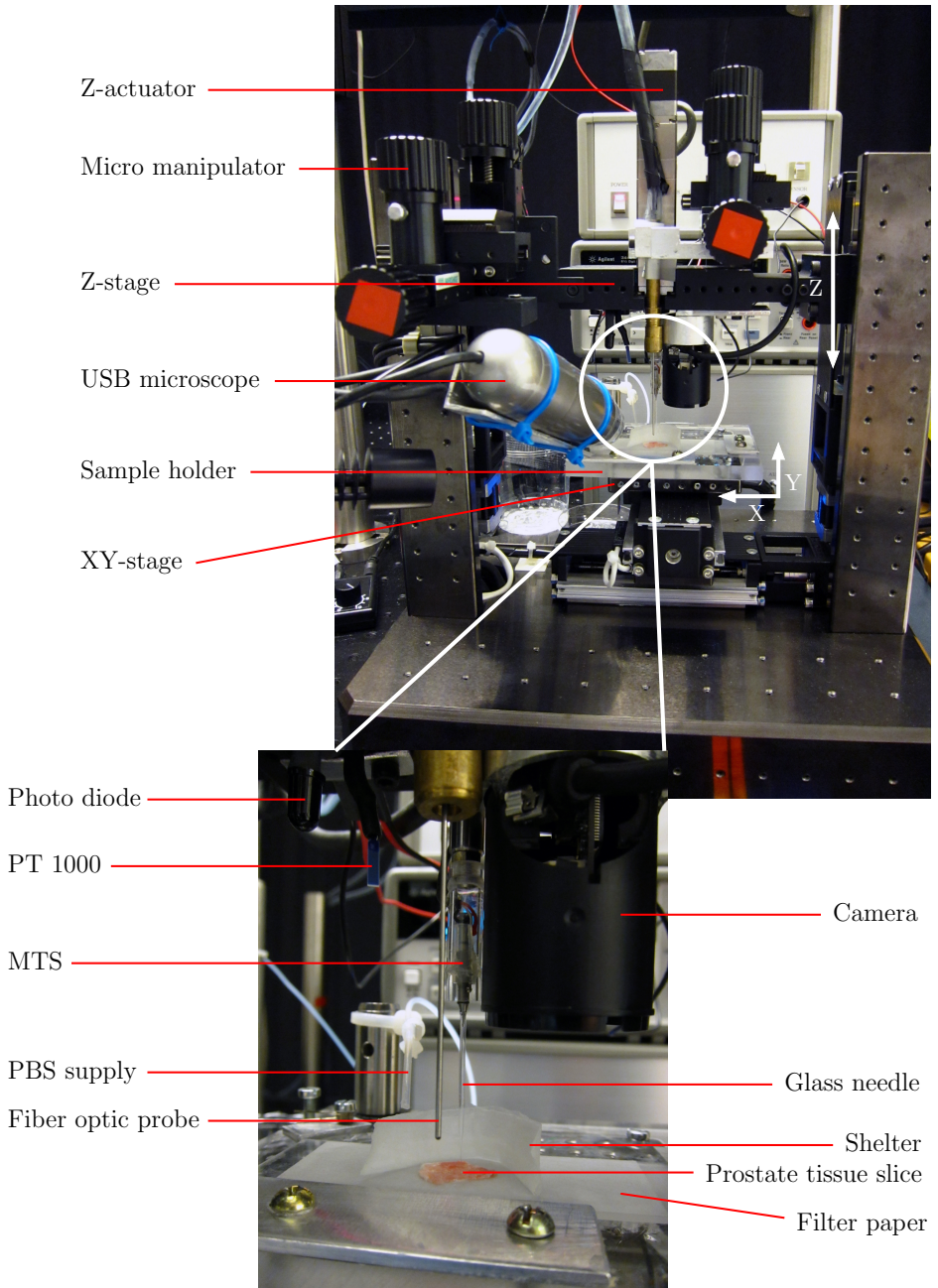
Shelter

Prostate tissue slice

Filter paper

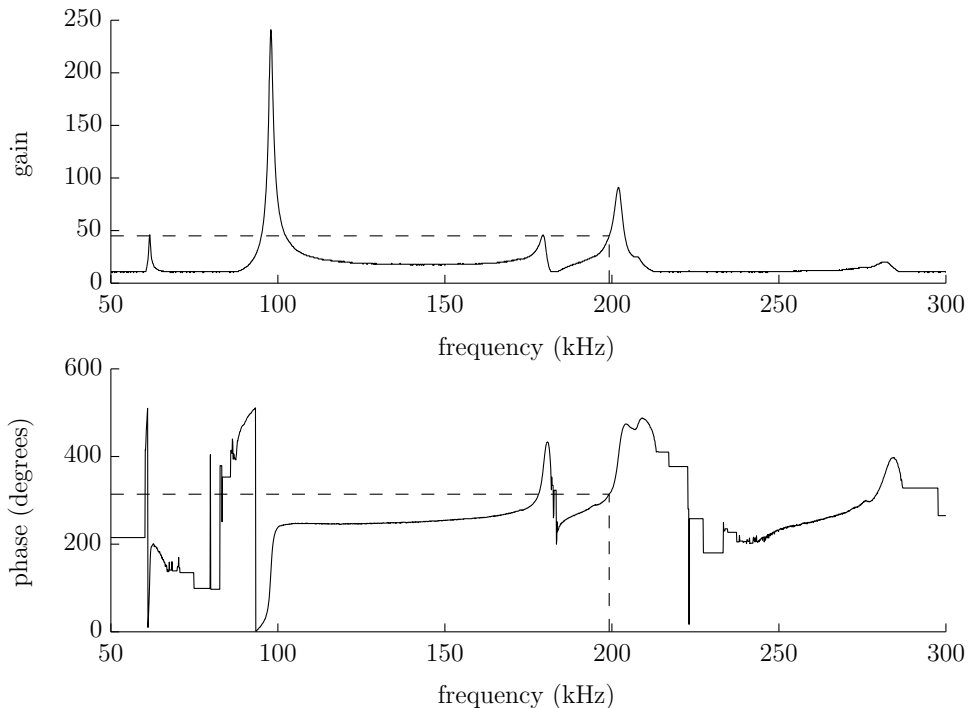*Figure 6.2: The experimental setup for Paper D.*

Figure 6.3: The gain- and phase characteristics for one of the sensors used in Paper D. The gain and phase for the selected frequency at 199.2 kHz are shown by the dashed lines. Usually a high sensitivity was obtained only in a narrow interval of a few kHz around a unique frequency. The best performance was often attained close to the second major peak in the gain-frequency curve (top), which usually was present at around 200 kHz.

6.3 Sample preparation

For the study of the effects of laser illumination and snap-freezing (B) two porcine prostates were removed from boars slaughtered at the local abattoir. The prostates were enclosed in a plastic bag and refrigerated. The prostates were not removed from the urethra and the surrounding, protective tissue until cut into smaller samples, which was done within 24 hours after slaughter. Samples were either stored in PBS in the refrigerator (referred to as fresh samples), or snap-frozen in liquid nitrogen and stored at $-80\,°C$. The frozen samples were allowed to passively thaw immersed in PBS prior to measurement.

In Paper C pork belly tissue was used as a model system. Two pieces were obtained from the local grocery store. They were stored at $6\,°C$. Two samples were cut from each piece, for a total of four samples. The samples were placed on a Styrofoam plate, which was fastened to the translation stage, as shown in Figure 6.1.

In Paper D both porcine and human prostate tissue were investigated. Eight porcine
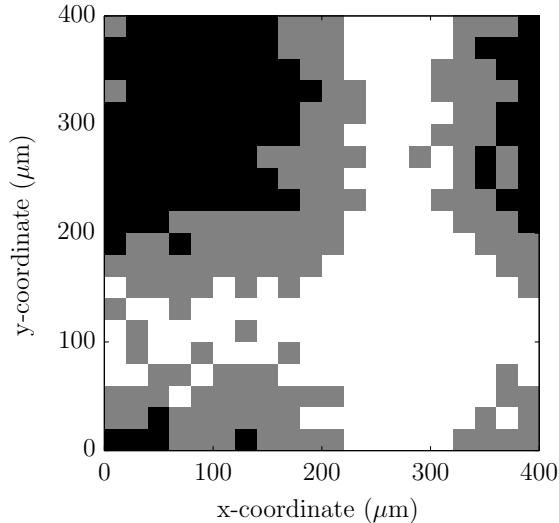
Figure 6.4: An example of a cluster analysis of RS data from a mapping over the line intersection used as reference mark for spatial calibration.

prostates were collected from slaughtered boars. They were cut into smaller pieces, which were snap-frozen and cut into 500-μm thick slices using a freezing microtome. Adjacent to both sides of each slice 5-μm thin specimens were cut. They were stained for histological analysis. Small samples retrieved from the prostate of a patient undergoing radical prostatectomy were snap-frozen in liquid nitrogen within thirty minutes after surgery. They were prepared in the same way as the porcine samples. Three of the samples contained cancerous tissue and were included in the study. All samples were stored at $-80\,°C$ until measured.

6.4   Measurement procedure

To study the effects of laser illumination, repeated Raman spectra were acquired from the same point on the fresh tissue samples (B). The integration time was set to 10 s to capture rapidly occurring effects. Spectra were captured subsequently during the first minute, then less frequently during the following four minutes. For the snap-freezing experiments five samples were measured day 1 and used as reference for fresh samples (B). Five snap-frozen samples were measured after 5, 26 and 81 days of storage, to study if prolonged storage at $-80\,°C$ degraded the tissue. The samples were immersed in PBS during the measurements.

For the combined TRM and RS measurements on pork belly tissue, a grid with 42 measurement points was defined for each sample (C). In total 168 points were measured with each device. The measurement order was randomized with the constriction that

adjacent points were not measured subsequently. This avoided the possibility that viscoelastic effects would influence the TRM measurements. All TRM measurements on a sample were completed before the acquisition of Raman spectra. The tissue was kept moist by brushing it with PBS every fifth minute. The distance from the RS probe to the sample had to be adjusted manually. A magnifying glass was used to facilitate the adjustment.

For the combined measurements on porcine and human prostate tissue (D) dehydration was prevented by putting the samples on a filter paper soaked with PBS, which was put on top of a microscope slide with low spectral background (Calcium Fluoride UV grade, Crystran Ltd., Poole, UK). A shelter made from a rolled-up piece of a Kimwipe paper (Kimtech Science Kimwipes, Kimberly-Clark Inc., Roswell, GA, USA) was put around the sample, and a constant flow of PBS was applied to it (Figure 6.2). The user set the measurement region of interest in the labview™ program. The MTS was set to the starting position and the surface was detected through the frequency shift. A stiffness map and a topography map were then acquired with the MTS. The step size was 50 μm. Next the RS probe was moved to the starting position and a Raman map was captured using a 300 μm step size. The distance from the RS probe to the sample was adjusted to be constant at 400 μm by using the topography map recorded by SHM.

6.5   Data analysis and statistics

All data analysis was performed using matlab® (version R2007b/R2008b/R2010a including Statistics Toolbox version 6.1/7.0/7.3, MathWorks Inc., Natick, MA, USA). The only exception was that minitab® (version 15.1.20.0, Minitab Inc., State College, PA, USA) was used to check for autocorrelation in Paper B. The algorithms not included in matlab® were written in-house.

The RS data was preprocessed as follows (B–D). The Fingerprint region from 400–1800 cm^{-1} was selected. Wavelengths < 600 cm^{-1} were excluded due to interfering Raman scattering generated in the fiber optic probe (C, D) [92]. Spectral spikes due to cosmic rays were removed prior to analysis. Correction for the energy sensitivity of the spectrometers was applied. Each Raman spectrum was lightly filtered using the smoothing algorithm by Eilers [126]. The background was automatically subtracted via the algorithm by Cao et al. [97]. To aid comparison the spectra were vector normalized, so that their integrated areas were equal. In Paper D the variance minimization method [127] was used to remove the Raman signal generated in the fiber optic probe and the interfering signal from the filter paper. The Raman spectra were interpreted by making tentative assignments of the peaks. The database collected by Movasaghi et al. [98] was frequently used. PCA was applied to the preprocessed Raman spectra to reduce the dimensionality of the data (B, C). It was performed on unstandardized data, i.e. the variables were not scaled by dividing them by their standard deviations. The ten first PCs were retained for further evaluation. They explained a large percentage of the total variance.

In Paper B a modified version of Kim's test [128, 129] was used to determine if the multivariate means of the PC scores of fresh and snap-frozen tissue differed. Three

analogous analyses were conducted, fresh tissue was compared to snap-frozen tissue stored at $-80\,°C$ for 5, 26 and 81 days. If the test showed a significant difference, Yuen's univariate test [130] was applied to compare the means of the individual PC scores. This was done to investigate which PCs that contributed strongly to the significant multivariate difference. The spectra of these PCs showed the main spectral differences between fresh and snap-frozen tissue.

In Paper C the Raman PC scores were input to an unsupervised HCA algorithm using Ward's linkage [116, 117]. The data set included all 168 spectra. The cluster analysis divided the spectra into five groups. They were labeled A, B, C, D and E in Paper C, and will here be represented by different colors: black, green, gray, red and blue, respectively. The TRM stiffness-sensitive parameter $\partial F/\partial \Delta f$ was calculated from Δf, F and d as [19]

$$\frac{\partial F}{\partial \Delta f} = \frac{\partial F/\partial d}{\partial \Delta f/\partial d} \tag{6.1}$$

and evaluated at $d = 0.6 \pm 0.1$ mm using linear regression (C). At this depth the sensor measures the tissue near the surface [19]. The nonparametric Kruskal-Wallis test followed by Tukey-Kramer's multiple comparison test were used to test if the mean stiffness of the groups differed. To evaluate the relationship between the TRM and RS information a linear regression analysis was conducted using the Raman PC scores to explain the stiffness variation. Furthermore, receiver operating characteristic curves were constructed to investigate the ability of TRM to classify each tissue type defined by the cluster analysis of RS data. They showed the sensitivity and specificity for distinguishing the current tissue type from the others for varying stiffness threshold values.

In Paper D three main tissue types were identified in the histologic analysis of the porcine samples: epithelium, lumen and stroma. For the human samples the groups were: epithelium, lumen, stroma, cancerous epithelium, cancerous stroma and prostate stones. The stiffness sensitive parameter for the MTS, $\Delta f/\delta$, was calculated in MATLAB$^®$. Furthermore, a measure of nonlinear effects was calculated by fitting a second-degree polynomial to the frequency versus indentation curve for each measurement. Differences in the biochemical composition of the tissue types were assessed by analyzing the mean spectra of the tissue types. The Kruskal-Wallis and Tukey-Kramer tests were used to test for significant differences in stiffness. An SVM analysis was performed to find the accuracy of using the TRM alone, and TRM and RS together, to classify the tissue types. Different degrees of tissue homogeneity were analyzed (D).

A p-value less than 0.05 was considered as statistically significant for all statistical tests. It was assumed that the experimental designs were completely randomized and that the observations were independent.

General Results and Discussion

This chapter summarizes and explains the findings in Papers A–D, and discusses their relevance for the development of an instrument combining TRM and RS for PCa detection.

7.1 Literature review

The gold standard for PCa detection and diagnosis, the PSA test and SB, lacks sensitivity and specificity (A). Indolent and aggressive tumors cannot be reliably differentiated, and the rate of overtreatment is high (A).

Grey-scale transrectal ultrasound is used only to guide biopsies to predetermined sites according to SB protocols, since tumors usually cannot be discerned on the ultrasound image. Ultrasound techniques that assess the prostatic blood flow or tissue elasticity are more effective (A). The best results have been obtained with contrast-enhanced ultrasound. Directing biopsies at suspicious lesions detects more clinically significant tumors with fewer biopsy cores, as compared to SB [12, 131, 132]. However, ultrasound methods still show a low specificity. The subjective interpretation is also a limitation [12].

Advanced MR techniques are very promising (A). The specificity of T2-weighted MRI is merely 50%, but it can be increased significantly by the addition of MRSI [11, 133]. A meta-analysis of the literature showed that the sensitivity and specificity of MRSI for PCa detection are 64% and 86%, respectively [134]. MRSI offers objective detection of PCa based on the elevated tumor metabolism. The combination of MRI and MRSI has attained high detection accuracies in many studies. Dynamic contrast-enhanced MRI significantly increases the detection rate of conventional MRI [11]. Diffusion weighted imaging may also improve MRI performance [133]. A combination of several MR techniques has the potential to detect most tumors of clinical significance [133]. The first studies of multiparametric MRI show promising results [135–137]. The main drawbacks of MRI are high costs, limited availability of MR scanners and that MR-guided biopsy is a complex procedure [11, 138].

Computer-aided detection and diagnosis is expected to play an important role in the future (A). Intra- and interobserver variability is an issue with both ultrasound and MR techniques. Computerized interpretation have the potential to objectively and efficiently analyze the huge amounts of data generated by new advanced techniques.

Paper A shows that there is a need for new cost-effective and complementary methods for localization and diagnosis of PCa. In particular, it is important to distinguish indolent and aggressive PCa. The proposed instrument combining TRM and RS is interesting as a complementary method for PCa detection, since the individual techniques have demonstrated promising results in vitro (A). However, Paper A concluded that the penetration depth of RS is currently insufficient for noninvasive detection of PCa. Thus, at the present time it is foremost during radical prostatectomy that the combined instrument can make a difference. If the surgical margins can be cleared from cancerous tissue, cancer recurrence could be minimized and adjuvant therapy may be unnecessary, even for men with high-risk tumors. A miniaturized version of the combined instrument could also play a role in biopsy procedures, by analyzing the tissue in proximity to the tip of the needle, and point out regions suspicious for cancer.

7.2 Effects of snap-freezing and laser illumination

7.2.1 Laser illumination

The analysis of difference spectra showed that no changes in the Raman spectra occurred due to the laser illumination ($n = 5$) (B). The intensity of the background decreased with the laser illumination time, while the intensity of the Raman signal was unaltered (Figure 7.1). The results were similar for all measurement series. The discussion in Paper B indicates that photobleaching of tissue fluorophores caused the decrease of background intensity. Porphyrins present in myoglobin and hemoglobin were the most likely sources of autofluorescence. If the background is removed during preprocessing of Raman data, this phenomenon should not affect the spectral information significantly.

This study shows that the in vitro measurement protocol was appropriate. NIR illumination of high irradiance did not seem to harm the tissue under the given experimental conditions. For in vivo measurements, the probed tissue will not be immersed in PBS and may not withstand such a high irradiance. However, the irradiance from a fiber optic system will usually be much less than from a microscopic system, due to a larger illumination area, and living tissue may be heat-resistant due to circulating, cooling blood [92]. Hattori et al. [92] used an RS fiber optic probe of the same type used in Paper C to measure the esophagus and stomach of rats in vivo. They found no evidence of degradation of the tissue at an excitation power onto the sample of 80 mW. Assuming that the excitation area equals the area of the delivery fiber ($\varnothing = 125~\mu$m), this corresponds to an irradiance of about $\sim 7 \cdot 10^6$ W m^{-2}, which can be compared to the irradiance $\sim 3 \cdot 10^{10}$ W m^{-2} for the system used in Paper B.

7.2.2 Snap-freezing

Multivariate tests showed that there was a significant difference ($p < 0.05$) between the spectra of fresh and snap-frozen tissue (B). The main spectral differences were found through univariate tests of the difference between the PC scores of fresh and snap-frozen
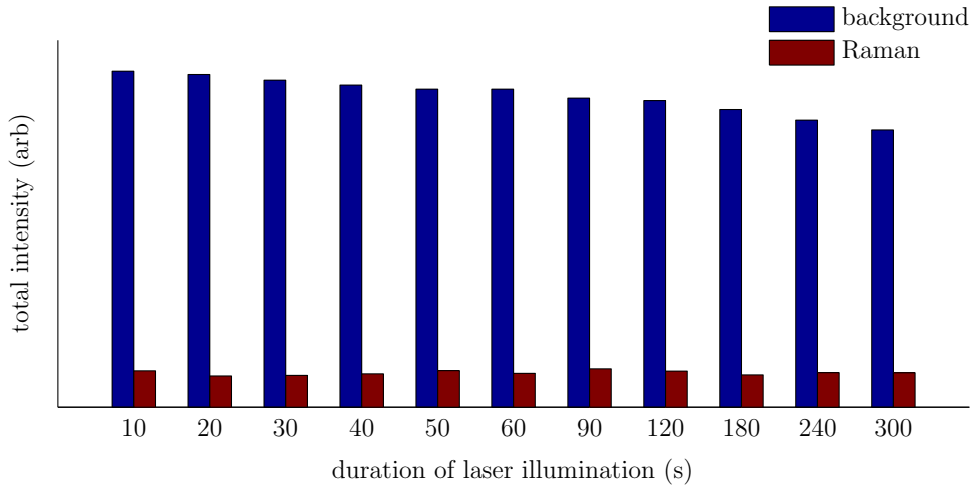
Figure 7.1: The total intensity of the spectral background decreased with the laser illumination time, whereas the intensity of the Raman signal showed small random fluctuations.

tissue, see Table 1 in Paper B, and analyses of the corresponding PCs (Figure 7.2). Some common effects due to the snap-freezing can be listed:

❐ Decreased intensity of the phenylalanine (1006 cm^{-1}) and tryptophan (1548 cm^{-1} and 760 cm^{-1}) peaks.

❐ The amide I peak (1654–1685 cm^{-1}) is shifted towards lower wavenumbers.

❐ Increased intensity at $\sim$ 1441 cm^{-1} and $\sim$ 1299 cm^{-1}, which was assigned to CH$_2$/CH vibrations of lipids and/or proteins.

❐ The amide III peak at $\sim$ 1244 cm^{-1} is decreased.

The changes due to snap-freezing were subtle and could not be revealed by comparing mean spectra. Figure 7.3 shows two spectra for day 26 where the differences were relatively large. Significant differences between tissue samples stored at $-80\,°$C for different time-spans were found, indicating that the tissue may be affected by the storage. However, the p-values were much larger (of the order of 10^2–10^6 times larger) than those found comparing fresh and snap-frozen tissue. Thus, it was most likely the snap-freezing or thawing, and not the storage at $-80\,°$C, that was the main cause of the observed changes. As discussed in Paper B, the changes caused by snap-freezing were probably related to alterations of the protein conformation. This may be important to consider for studies that use snap-freezing and find diagnostic information related to protein conformation. Since the changes in cancerous prostate tissue mainly seem to be related to DNA and lipids [24, 27, 99], these findings suggest that snap-freezing may be used to study the difference between healthy and cancerous prostate tissue in vitro.
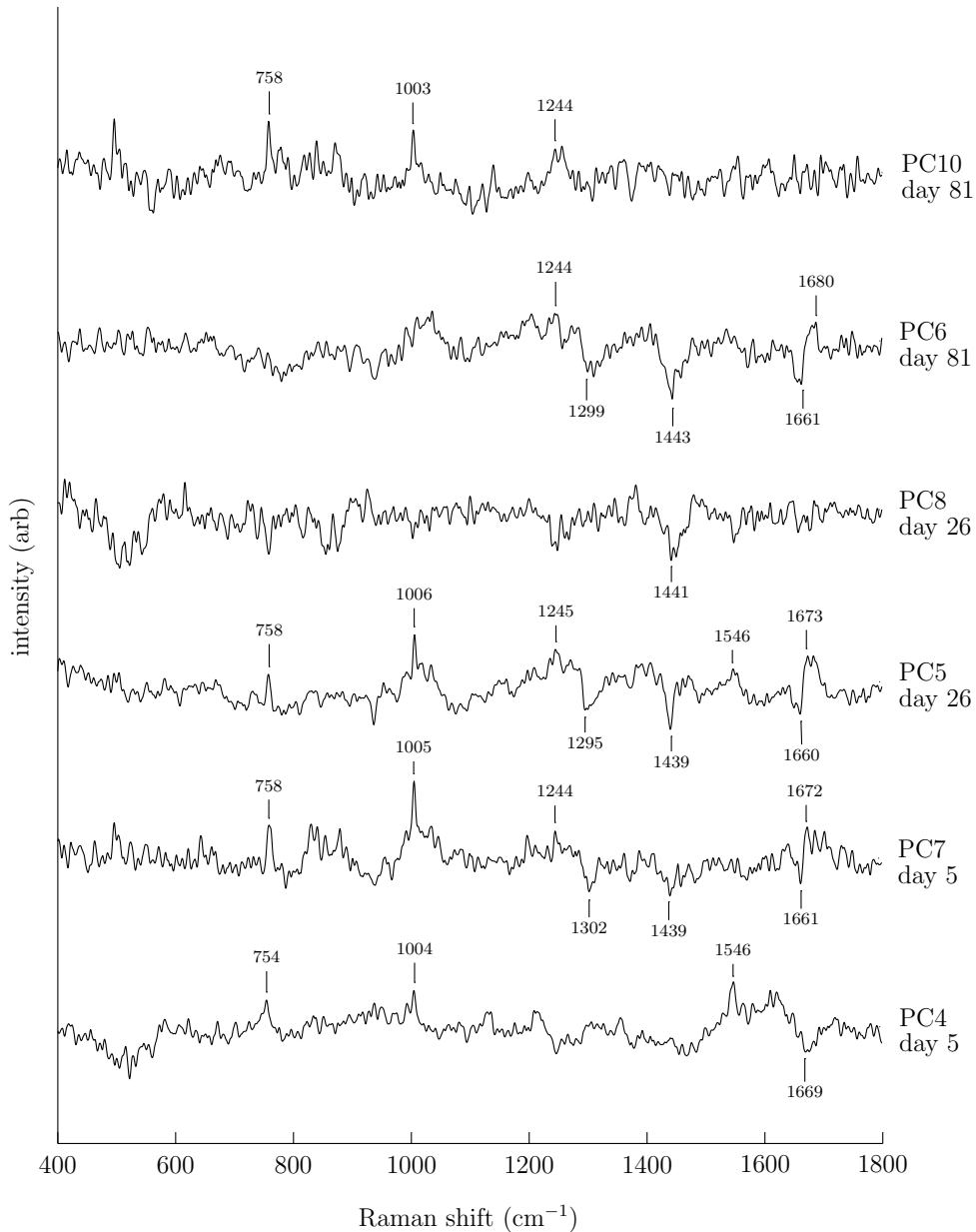
Figure 7.2: The calculated PCs whose scores were proven to be significantly different for fresh and snap-frozen tissue. Fresh tissue obtained higher scores for these PCs. Peaks characteristic for the differences have been labeled with their wavenumbers.
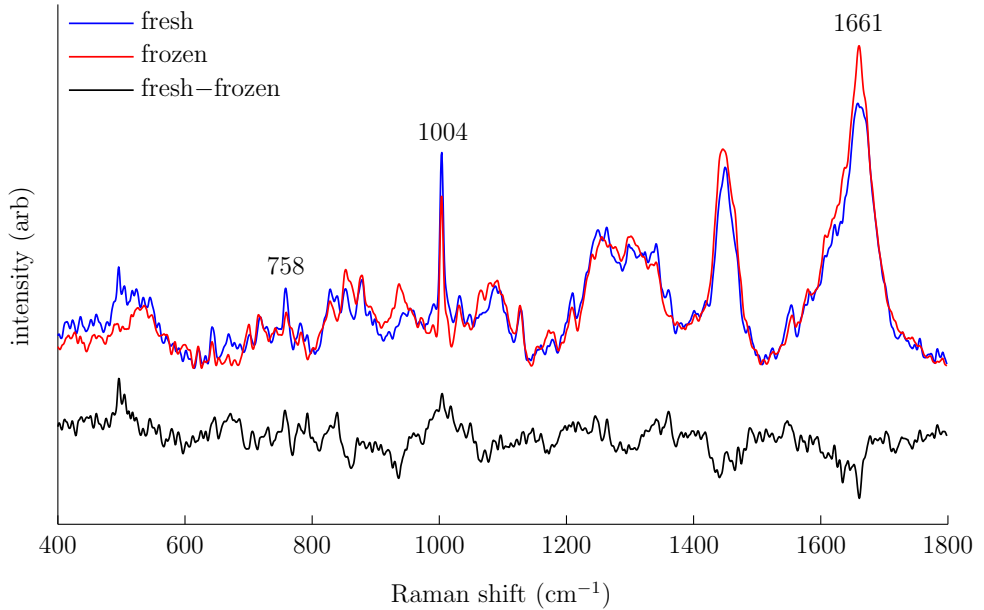
Figure 7.3: A spectrum on fresh as compared to snap-frozen prostate tissue for day 26. The difference between the spectra is plotted in black.

7.3   Comparing TRM and RS information

Figure 7.4 shows the result of the cluster analysis of the PC scores of the RS data for one of the samples (C). Visual inspection showed that the spots marked with black were muscle tissue, the red and blue groups fat tissue, whereas the gray and green groups were a mix of muscle and fat tissue. This was confirmed by analysis of the Raman spectral data (C). Figure 7.5 shows the mean spectrum of each group. Analysis of the spectral peaks showed that the blue group contained a higher amount of saturated fatty acids than the red group (C). The spectra were clustered into distinct groups. PC 1, PC 2 and PC 4 contributed strongly to the clustering (Figure 7.6). The interpretations of them were that PC 1 was related to the proportion of fat, PC 2 to the proportion of protein, and PC 4 to the composition of the fat.

The mean stiffness of each tissue group was calculated from the TRM measurements (C), see Figure 7.7. The blue group was significantly stiffer than the other groups ($p < 0.05$). It was explained by the difference in the composition of the fat shown by RS (C). In general, saturated fatty acids have higher melting points than unsaturated fatty acids [139]. Thus, the stiffness is related to the portion of saturated fat.

As shown in Table 1 in Paper C, the RS data explained 67% ($R^2_{\mathrm{adj}} = 0.67$) of the total variability of the stiffness parameter. PC 2 and PC 4 were the most important predictor variables, indicating that the proportion of fat and its composition contributed most
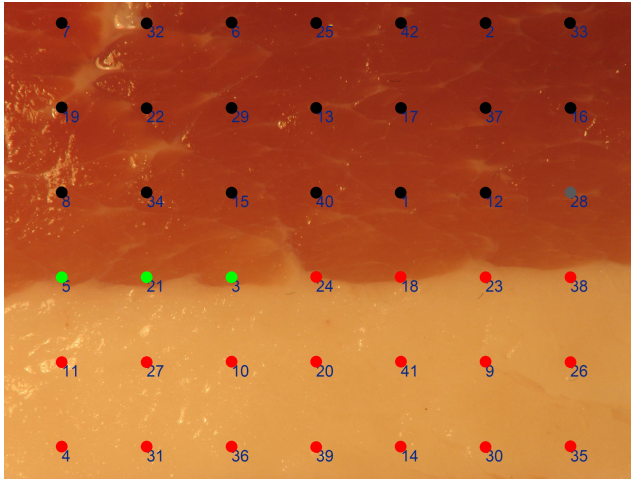
Figure 7.4: The outcome of the clustering analysis for one of the pork belly samples. The grid overlay shows the 42 measurements points. The measurement order is shown by the numbers. The group assignment is indicated by the colors. One of the groups (blue) was not represented in this sample. The light area of the sample consisted of fat tissue and the dark area was muscle tissue.
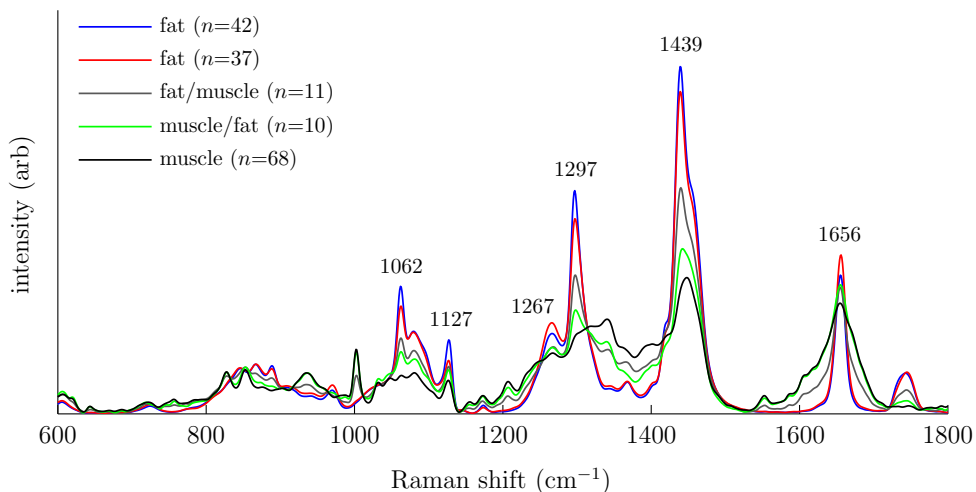

Figure 7.5: The mean spectra of the pork belly tissue groups, which were defined by the cluster analysis. The peaks whose intensity differed substantially between the two fat groups have been labeled with their wavenumbers.

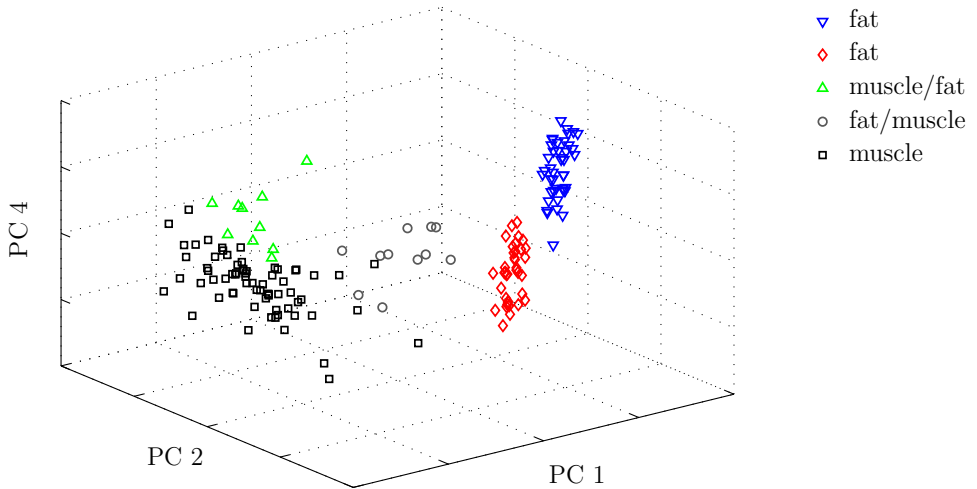*Figure 7.6: A scatter plot of the scores of PC 1, PC 2 and PC 4 for all RS measurements on the pork belly samples. The colors represent the group assignment from the cluster analysis.*
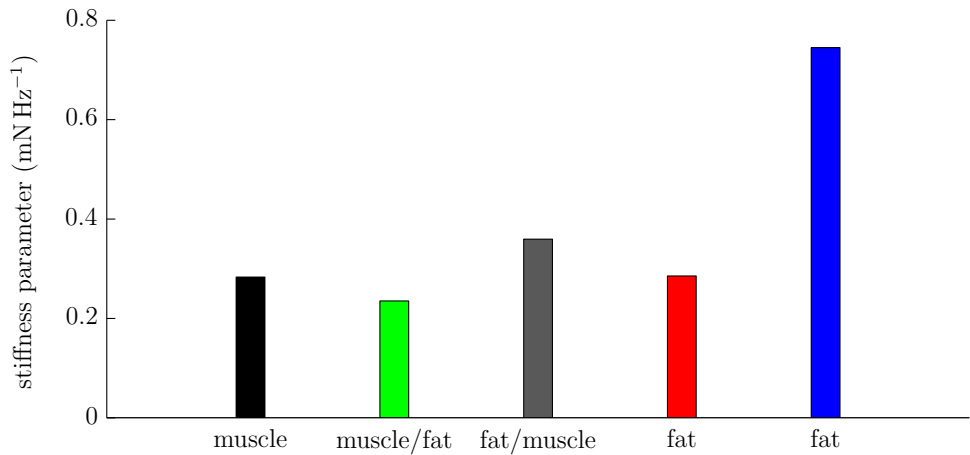

Figure 7.7: The mean stiffness of the five groups defined by the cluster analysis of RS data. A high value indicates a higher stiffness. The blue fat group was significantly stiffer than the other groups ($p < 0.05$).

to tissue stiffness. The analysis of the receiver operating characteristic curves showed that the fat group that was stiffest (blue) was satisfactorily identified using TRM (C). However, the accuracies for identifying the other groups were lower. The Venustron® sensor measured a much larger volume than the RS probe (C). This may partly explain why TRM obtained a relatively poor differentiation of the tissue groups. The TRM sensor probed a mix of several tissue types in many cases, while the RS probe usually measured a more homogeneous area.

In summary, Paper C shows that the TRM and RS information can be compared without prior knowledge of the tissue by a multivariate approach. The method uses PCA and HCA to identify different tissue types at a chosen level of detail. Next, linear regression is used to relate the stiffness to the biochemical composition, and receiver operating characteristic curves assess how the stiffness information can be used to classify the tissue types. As shown in Paper C the method was able to extract a relationship that was not initially suspected, namely that there was a difference in stiffness between two visually similar tissue types, and that it could be explained by the difference in the amount of saturated fat. Furthermore, it showed that the biochemical information obtained from the RS measurements provided additional discriminatory power to the TRM.

7.4   Classification of prostate tissue

Figure 7.8 shows a typical example of an SHM mapping measurement of porcine prostate tissue, and Figure 7.9 shows one of the mappings on human tissue. For most samples the structures observed in the histology image were clearly reproduced in the stiffness map. The statistical tests showed that the mean stiffness of the porcine tissue types differed ($p < 0.05$). Stroma was stiffest, whereas lumen was softest. Comparison of the mean spectra (Figure 7.10) indicated that the amount of collagen was highest in stroma and lowest in lumen (D). Thus, it is likely that collagen contributes substantially to prostate tissue stiffness. For the human samples the statistical tests showed that lumen was significantly softer than the other tissue types, except for healthy epithelium. This agrees well with the results for porcine tissue. It was also shown that prostate stones were significantly stiffer than cancerous epithelium, healthy stroma, and lumen. That prostate stones are very stiff has been shown by Jalkanen et al. [20] and Eklund et al. [37]. Interestingly, the median stiffness value for cancerous stroma was higher than the healthy tissue types, although it was only significantly stiffer than lumen. This suggests that cancerous stroma may be a cause to the increased stiffness due to PCa.

From the SHM measurements it was observed that there was a predictive value in the shape of the measurement curve, i.e. the degree of nonlinearity (D). The curvature of the measurement curves for the tissue types differed (Figure 7.11). The difference was significant ($p < 0.05$). The classification accuracy was substantially increased when this variable was added to the SHM data. Furthermore, the SHM measurements on human tissue indicated that this parameter added complementary information for tissue discrimination (D). Cancerous stroma showed a significantly higher ($p < 0.05$) deviation from linearity than all healthy tissue types (D). Moreover, cancerous epithelium could be
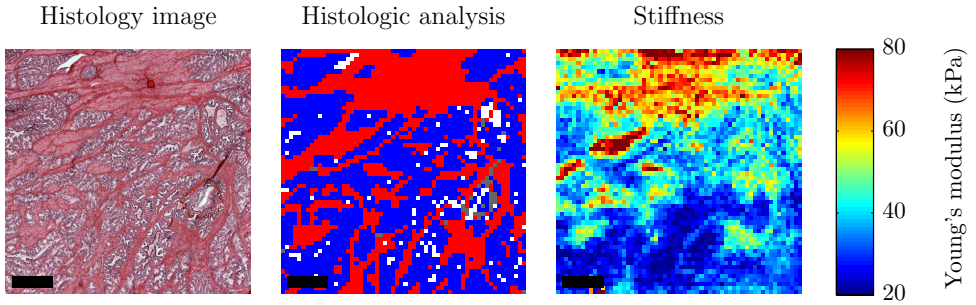
Figure 7.8: Results for one of the SHM measurements on porcine prostate tissue. In the histologic analysis image epithelium is shown in blue, lumen is white, and stroma is red. The gray points indicate that the tissue type could not be determined. The scale bars show 500 μm.
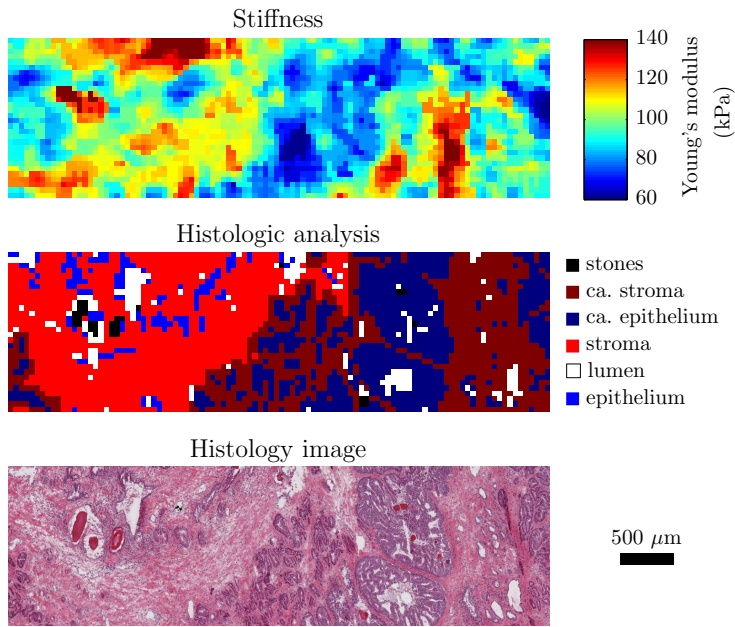
Figure 7.9: Results for one of the SHM measurements on human prostate tissue. The stiffness map has been noise-reduced using a median filter with a square kernel of 3×3 pixels. We see that the cancerous region to the right is associated with increased stiffness. Furthermore, healthy regions rich in stroma are relatively stiff. The area with stones is very stiff. The upper left portion of the sample showed signs of prostatic inflammation at high magnification. This may have increased the stiffness in this region. ca = cancerous.

Figure 7.10: The mean spectra of the porcine tissue types. The largest differences were found at the labeled peaks, which were all assigned to collagen (D).

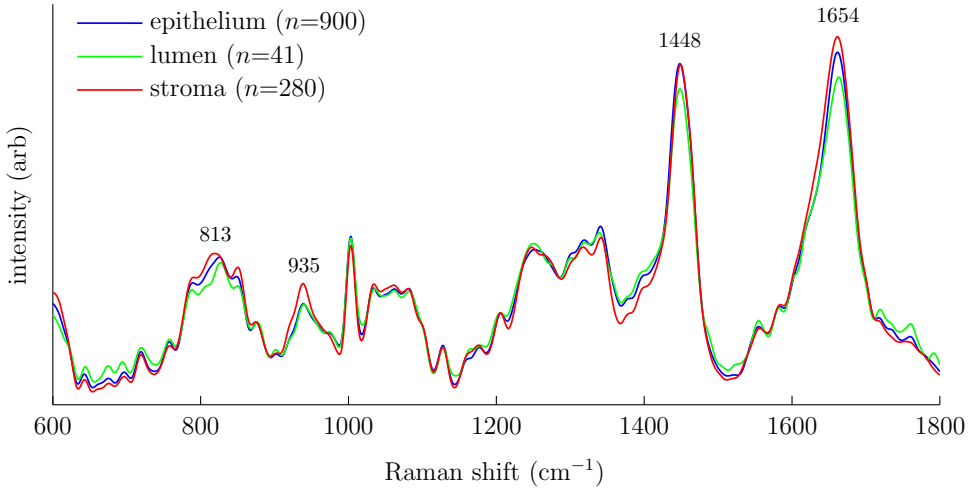distinguished from lumen and healthy epithelium ($p < 0.05$). This finding casts new light on the possibilities for tissue characterization using TRM alone. There may be additional diagnostic value, besides the stiffness calculated from the slope of the measurement curve, in the raw data. Further studies are necessary to explain the origin of the nonlinear effects, and assess their possible diagnostic value.

The spectral quality of the RS measurements on human samples was low (D). The reason was that the surgical margin of the removed prostate was covered with blue ink. This is standard clinical procedure; it is useful for determining if all cancerous tissue was removed at radical prostatectomy [17]. If cancerous tissue is found to be in contact with the inked margin, the patient is defined to have a positive surgical margin. The ink gave rise to very strong fluorescence that often saturated the detector in the Fingerprint interval, and swamped the Raman signal from the tissue. Fortunately, it was possible to partly overcome this problem by analyzing the high wavenumber region from 2400–3425 cm^{-1}, where the fluorescence was decreased. Although this region does not contain as much biochemical information as the Fingerprint region, the diagnostic value may be similar [86–88]. We found that almost as high classification accuracies were attained for the porcine samples using the high wavenumber region, as compared to the Fingerprint region. However, in comparison with the spectra of porcine tissue the spectral quality was lower for human tissue in the high wavenumber region. Spectra of human tissue were considerably more noisy. Thus, we believe that important diagnostic information may have been lost due to the strong fluorescence.

Figure 7.12 presents the SVM classification accuracies for distinguishing healthy porcine tissue types, and for distinguishing healthy and cancerous prostate tissue, for different
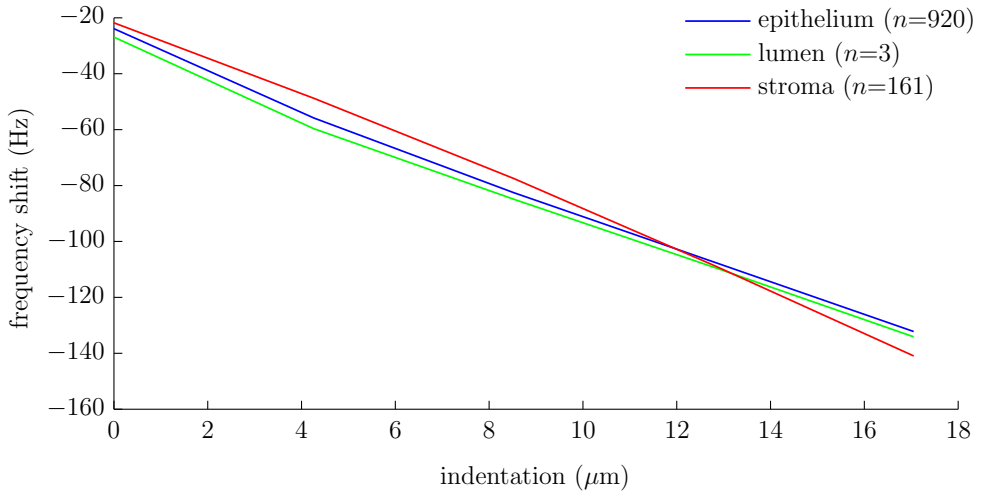
Figure 7.11: The mean SHM measurement curves, for points in homogeneous tissue regions, for the different tissue types for one of the porcine samples. We see that the measurement curves show slight deviations from linearity, and that the curvature for stroma differs from epithelium and lumen.

degrees of tissue homogeneity. TRM alone attained a high accuracy for distinguishing different porcine tissue types, especially for the most homogeneous tissue regions when it was 82%. In combination with RS the accuracy was $> 80\%$, even when the most heterogeneous tissue regions were included in the analysis. For differentiating cancerous tissue the accuracy was 67–70% when using the TRM alone. The analysis of the SHM data indicated that the overlapping stiffness distributions of healthy stroma and cancerous epithelium may have been the main limiting factor (D). The accuracy was increased to 73–77% when RS was added to SHM. The combined accuracy would most likely have increased if the spectral quality for human tissue would have been higher. In future studies alternative experimental approaches should be considered, in order to eliminate or decrease the interference from the application of ink to the surface of the removed prostates.

The results of Papers C and D clearly show that it is feasible and valuable to combine TRM and RS for tissue characterization. Used as a research tool the combination shows promise to extract unknown relationships between stiffness and biochemical composition by the multivariate approach presented in Paper C. This may help to explain the cause for changes in tissue stiffness due to cancer. For the development of a clinical instrument for probing surgical margins Paper D indicates that there is diagnostic information for distinguishing healthy and cancerous tissue using TRM alone. With the addition of RS the diagnostic power is increased. The combination shows high potential for exact tissue characterization, even in complex tissue regions with a mix of different tissue types. This is very promising for the development of a clinical tool to be used during PCa surgery.
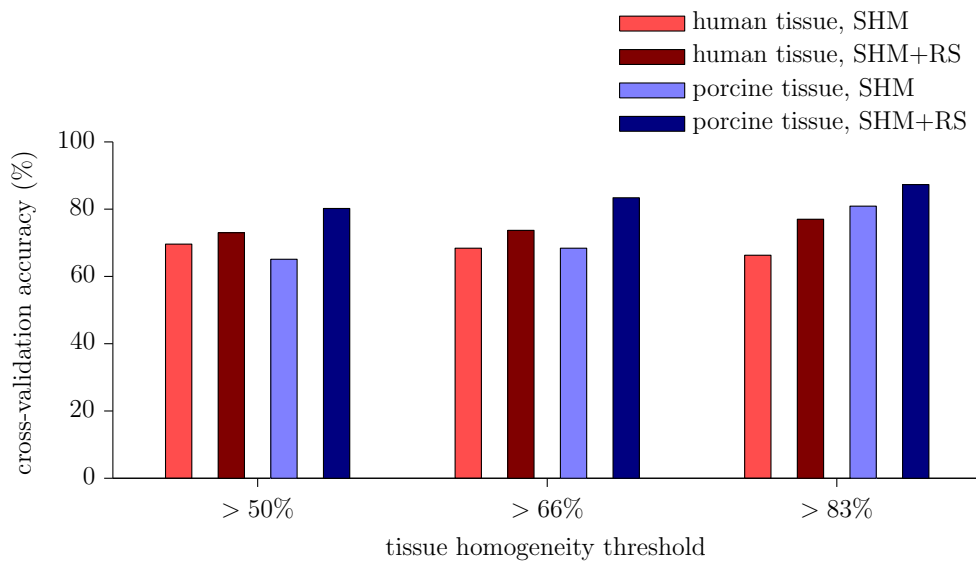
Figure 7.12: The five-fold cross-validation accuracies for SVM classification of the porcine prostate tissue types epithelium, lumen and stroma, and healthy and cancerous human prostate tissue.

CHAPTER 8

General Summary and Conclusions

This thesis reviewed the current state–of–the–art in PCa detection. The importance of appropriate in vitro preparation protocols and measurement procedures was discussed and evaluated, and the effects of snap-freezing and NIR laser illumination on porcine prostate tissue were investigated using RS. The combination of TRM and RS was evaluated in experiments on porcine and human tissues using multivariate techniques for explaining the data correlation and assessing the potential for characterization of healthy and diseased tissue.

From the review it was concluded that the specificity and sensitivity of clinical methods currently used for PCa detection and diagnosis, the PSA test and SB, are insufficient. Indolent and aggressive tumors cannot be reliably differentiated, which results in many men being treated either unnecessarily or too late. Clinical benefits of state–of–the–art technology for PCa imaging, advanced ultrasound and MR techniques, have still not been convincingly shown. There is a need for complementary and cost-effective detection methods. TRM and RS are promising complementary techniques.

In the RS study no indications of tissue degradation due to 830 nm laser illumination at an irradiance of $\sim 3 \cdot 10^{10}$ W m^{-2} were observed. Snap-freezing and subsequent storage at $-80\,^{\circ}$C gave rise to subtle but significant changes in the Raman spectra, most likely related to alterations in the protein conformations. Since the main changes in cancerous prostate tissue appear to be related to DNA and lipids, these findings indicate that snap-freezing may be used to preserve samples for in vitro studies concerning PCa detection.

The measurements on porcine and human tissue types showed that the combined data can be used to study the causes of differences in tissue stiffness through a multivariate approach. Furthermore, the classification accuracy of healthy porcine tissue types was high using TRM alone, and increased substantially when RS was added. The measurements on human tissue indicate that efficient detection of PCa may be possible.

To summarize, this thesis shows that a combined instrument incorporating both TRM and RS is a promising complementary method for PCa detection. Snap-freezing of samples may be used in future RS evaluations of changes in cancerous prostate tissue. The instrument has potential for assisting surgeons in cancer surgery, and for biopsy guidance. The goal is to provide a more secure diagnosis and consequently more efficient treatment of the patient.

Future Outlook

This thesis shows that a future instrument combining TRM and RS may be useful for tumor detection and diagnosis. The TRM sensor would be used to swiftly scan the tissue for stiff lesions. With the additional diagnostic power of RS it may be determined if a lesion is benign or malign, and whether it is indolent or aggressive. This could be accomplished in near real-time through computerized interpretation of measurement data. The combined instrument may be constructed by molding an RS fiber optic probe into a cylindrical resonance sensor element, as depicted in Figure 9.1. This is the thought device for probing surgical margins. Since the RS probe is shielded from surrounding light by the piezoelectric element, measurements may be performed in bright environments. The TRM sensor can be used for tactile feedback to the surgeons and inform them when the instrument touches the tissue. This would facilitate the practical clinical use.

A possible design for a miniaturized version of the combined instrument is shown in Figure 9.2. It uses a single optic fiber inserted into a hollow glass needle, as used for the MTS. This device could be used for possible guidance of prostate biopsies. By using RS measurements in the high wavenumber region it is possible to use a single optic fiber for spectral acquisition [86–88].

Although this thesis focused on PCa, the combined instrument could potentially be used for a variety of biomedical applications, both in vitro and in vivo. Both TRM and RS are versatile methods [18, 22], and the combination even more so, since biomechanical and biochemical information are retrieved simultaneously.
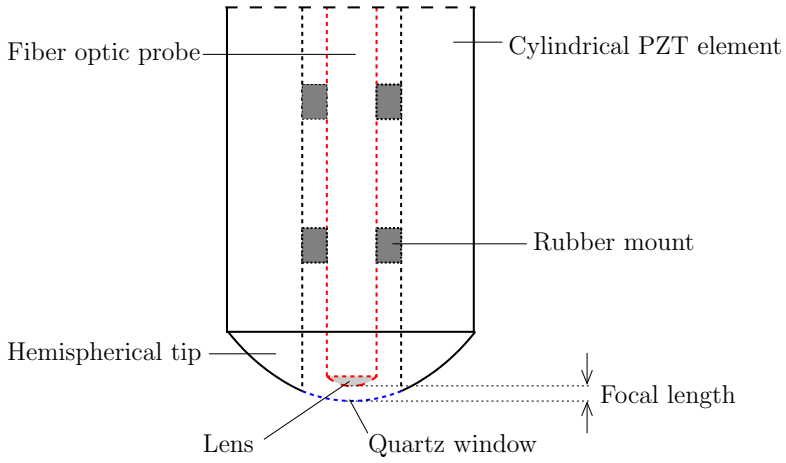
Figure 9.1: A possible design of an instrument for scanning of surgical margins.
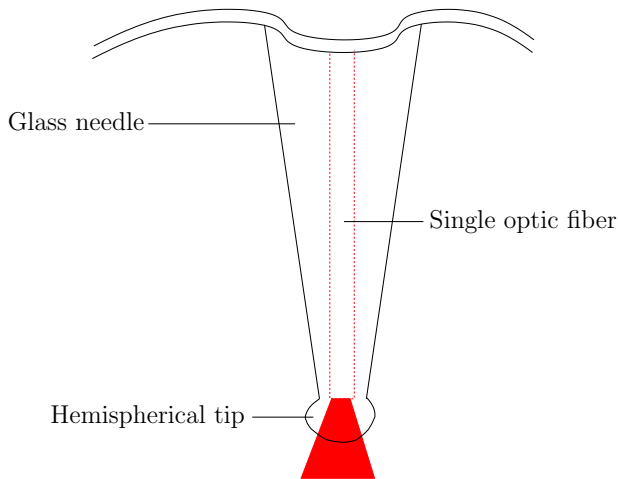

Figure 9.2: A possible design for a miniaturized instrument.

References

[1] J. Ferlay, D. M. Parkin, and E. Steliarova-Foucher, "Estimates of cancer incidence and mortality in Europe in 2008", *Eur J Cancer*, vol. 46, pp. 765–781, 2010.

[2] A. Jemal, R. Siegel, J. Xu, and E. Ward, "Cancer statistics, 2010", *CA Cancer J Clin*, vol. 60, pp. 277–300, 2010.

[3] S. A. Fedewa, R. Etzioni, W. D. Flanders, A. Jemal, and E. M. Ward, "Association of insurance and race/ethnicity with disease severity among men diagnosed with prostate cancer, National Cancer Database 2004–2006", *Cancer Epidemiol Biomarkers Prev*, vol. 19, pp. 2437–2444, 2010.

[4] N. J. Fitzsimons, L. Sun, and J. W. Moul, "Medical technologies for the diagnosis of prostate cancer", *Expert Rev Med Devices*, vol. 4, pp. 227–239, 2007.

[5] J. Hegarty, P. V. Beirne, E. Walsh, H. Comber, T. Fitzgerald, and M. W. Kazer, "Radical prostatectomy versus watchful waiting for prostate cancer", *Cochrane Database Syst Rev*, no. CD006590 (67 pp.), 2010.

[6] J. E. Johansson, L. Holmberg, S. Johansson, R. Bergström, and H. O. Adami, "Fifteen-year survival in prostate cancer – A prospective, population-based study in Sweden", *JAMA*, vol. 277, pp. 467–471, 1997.

[7] H. Hricak, P. L. Choyke, S. C. Eberhardt, S. A. Leibel, and P. T. Scardino, "Imaging prostate cancer: A multidisciplinary perspective", *Radiology*, vol. 243, pp. 28–53, 2007.

[8] F. H. Schröder, J. Hugosson, M. J. Roobol, T. L. J. Tammela, S. Ciatto, V. Nelen, M. Kwiatkowski, M. Lujan, H. Lilja, M. Zappa, L. J. Denis, F. Recker, A. Berenguer, L. Määttänen, C. H. Bangma, G. Aus, A. Villers, X. Rebillard, T. van der Kwast, B. G. Blijenberg, S. M. Moss, H. J. de Koning, A. Auvinen, and E. R. S. P. C. Investigators, "Screening and prostate-cancer mortality in a randomized European study", *N Engl J Med*, vol. 360, pp. 1320–1328, 2009.

[9] D. C. Fernandez, R. Bhargava, S. M. Hewitt, and I. W. Levin, "Infrared spectroscopic imaging for histopathologic recognition", *Nat Biotechnol*, vol. 23, pp. 469–474, 2005.

[10] J. E. McNeal, "Normal histology of the prostate", *Am J Surg Pathol*, vol. 12, pp. 619–633, 1988.

[11] A. P. S. Kirkham, M. Emberton, and C. Allen, "How good is MRI at detecting and characterising cancer within the prostate?", *Eur Urol*, vol. 50, pp. 1163–74; discussion 1175, 2006.

[12] L. Pallwein, M. Mitterberger, A. Pelzer, G. Bartsch, H. Strasser, G. M. Pinggera, F. Aigner, J. Gradl, D. Z. Nedden, and F. Frauscher, "Ultrasound of prostate cancer: recent advances", *Eur Radiol*, vol. 18, pp. 707–715, 2008.

[13] M. Fuchsjäger, A. Shukla-Dave, O. Akin, J. Barentsz, and H. Hricak, "Prostate cancer imaging", *Acta Radiol*, vol. 49, pp. 107–120, 2008.

[14] C. Sumey and T. W. Flaig, "Adjuvant medical therapy for prostate cancer", *Expert Opin Pharmacother*, vol. 12, pp. 73–84, 2011.

[15] B. Tareen, J. Kimmel, and W. C. Huang, "Contemporary treatment of high-risk localized prostate cancer", *Expert Rev Anticancer Ther*, vol. 10, pp. 1069–1076, 2010.

[16] Y. Yang, "Treatment of the positive surgical margin following radical prostatectomy", *Chin Med J*, vol. 121, pp. 375–379, 2008.

[17] O. Yossepowitch, A. Bjartell, J. A. Eastham, M. Graefen, B. D. Guillonneau, P. I. Karakiewicz, R. Montironi, and F. Montorsi, "Positive surgical margins in radical prostatectomy: outlining the problem and its long-term consequences", *Eur Urol*, vol. 55, pp. 87–99, 2009.

[18] O. A. Lindahl, C. E. Constantinou, A. Eklund, Y. Murayama, P. Hallberg, and S. Omata, "Tactile resonance sensors in medicine", *J Med Eng Technol*, vol. 33, pp. 263–273, 2009.

[19] V. Jalkanen, B. M. Andersson, A. Bergh, B. Ljungberg, and O. A. Lindahl, "Resonance sensor measurements of stiffness variations in prostate tissue in vitro – a weighted tissue proportion model", *Physiol Meas*, vol. 27, pp. 1373–1386, 2006.

[20] V. Jalkanen, B. M. Andersson, A. Bergh, B. Ljungberg, and O. A. Lindahl, "Prostate tissue stiffness as measured with a resonance sensor system: a study on silicone and human prostate tissue in vitro", *Med Biol Eng Comput*, vol. 44, pp. 593–603, 2006.

[21] V. Jalkanen, B. M. Andersson, A. Bergh, B. Ljungberg, and O. A. Lindahl, "Spatial variations in prostate tissue histology as measured by a tactile resonance sensor", *Physiol Meas*, vol. 28, pp. 1267–1281, 2007.

[22] C. Krafft, G. Steiner, C. Beleites, and R. Salzer, "Disease recognition by infrared and Raman spectroscopy", *J Biophotonics*, vol. 2, pp. 13–28, 2009.

[23] M. D. Keller, E. M. Kanter, and A. Mahadevan-Jansen, "Raman spectroscopy for cancer diagnosis", *Spectroscopy*, vol. 21, pp. 33–41, 2006.

[24] P. Crow, N. Stone, C. A. Kendall, J. S. Uff, J. A. M. Farmer, H. Barr, and M. P. J. Wright, "The use of Raman spectroscopy to identify and grade prostatic adenocarcinoma in vitro", *Br J Cancer*, vol. 89, pp. 106–108, 2003.

[25] P. Crow, B. Barrass, C. Kendall, M. Hart-Prieto, M. Wright, R. Persad, and N. Stone, "The use of Raman spectroscopy to differentiate between different prostatic adenocarcinoma cell lines", *Br J Cancer*, vol. 92, pp. 2166–2170, 2005.

[26] P. Crow, A. Molckovsky, N. Stone, J. Uff, B. Wilson, and L.-M. WongKeeSong, "Assessment of fiberoptic near-infrared Raman spectroscopy for diagnosis of bladder and prostate cancer", *Urology*, vol. 65, pp. 1126–1130, 2005.

[27] N. Stone, M. C. H. Prieto, P. Crow, J. Uff, and A. W. Ritchie, "The use of Raman spectroscopy to provide an estimation of the gross biochemistry associated with urological pathologies", *Anal Bioanal Chem*, vol. 387, pp. 1657–1668, 2007.

[28] A. Nijssen, S. Koljenović, T. C. B. Schut, P. J. Caspers, and G. J. Puppels, "Towards oncological application of Raman spectroscopy", *J Biophotonics*, vol. 2, pp. 29–36, 2009.

[29] S. Devpura, J. S. Thakur, F. H. Sarkar, W. A. Sakr, V. M. Naik, and R. Naik, "Detection of benign epithelia, prostatic intraepithelial neoplasia, and cancer regions in radical prostatectomy tissues using Raman spectroscopy", *Vib Spectrosc*, vol. 53, pp. 227–232, 2010.

[30] P. Matousek, "Deep non-invasive Raman spectroscopy of living tissue and powders", *Chem Soc Rev*, vol. 36, pp. 1292–1304, 2007.

[31] G. J. Tortora and B. Derrickson, *Principles of Anatomy and Physiology*. New York: Wiley & Sons, 11 ed., 2006.

[32] S. N. Rasmussen and P. Riis, "Rectal wall thickness measured by ultrasound in chronic inflammatory diseases of the colon", *Scand J Gastroenterol*, vol. 20, pp. 109–114, 1985.

[33] G. R. Cunha, A. A. Donjacour, P. S. Cooke, S. Mee, R. M. Bigsby, S. J. Higgins, and Y. Sugimura, "The endocrinology and developmental biology of the prostate", *Endocr Rev*, vol. 8, pp. 338–362, 1987.

[34] L. C. Costello and R. B. Franklin, "Prostatic fluid electrolyte composition for the screening of prostate cancer: a potential solution to a major problem", *Prostate Cancer Prostatic Dis*, vol. 12, pp. 17–24, 2009.

[35] R. Klimas, B. Bennett, and W. A. Gardner, "Prostatic calculi: a review", *Prostate*, vol. 7, pp. 91–96, 1985.

[36] J. D. Christian, T. C. Lamm, J. F. Morrow, and D. G. Bostwick, "Corpora amylacea in adenocarcinoma of the prostate: incidence and histology within needle core biopsies", *Mod Pathol*, vol. 18, pp. 36–39, 2005.

[37] A. Eklund, A. Bergh, and O. A. Lindahl, "A catheter tactile sensor for measuring hardness of soft tissue: measurement in a silicone model and in an in vitro human prostate model", *Med Biol Eng Comput*, vol. 37, pp. 618–624, 1999.

[38] M. Swindle and A. Smith, "Comparative anatomy and physiology of the pig", *Scand J Lab Anim Sci*, vol. 25, pp. 11–21, 1998.

[39] R. N. C. Aitken, "A histochemical study of the accessory genital glands of the boar", *J Anat*, vol. 94, pp. 130–142, 1960.

[40] M. Nicaise, H. Lauwers, and P. Simoens, "Morphological study of the development of the disseminate prostate in intact and castrated male pigs aged two to six months", *Acta Anat*, vol. 141, pp. 335–347, 1991.

[41] F. Bray, J. Lortet-Tieulent, J. Ferlay, D. Forman, and A. Auvinen, "Prostate cancer incidence and mortality trends in 37 European countries: an overview", *Eur J Cancer*, vol. 46, pp. 3040–3052, 2010.

[42] D. E. Neal, H. Y. Leung, P. H. Powell, F. C. Hamdy, and J. L. Donovan, "Unanswered questions in screening for prostate cancer", *Eur J Cancer*, vol. 36, pp. 1316–1321, 2000.

[43] M. Yin, S. Bastacky, U. Chandran, M. J. Becich, and R. Dhir, "Prevalence of incidental prostate cancer in the general population: a study of healthy organ donors", *J Urol*, vol. 179, pp. 892–895; discussion 895, 2008.

[44] V. Kundra, "Prostate cancer imaging", *Semin Roentgenol*, vol. 41, pp. 139–149, 2006.

[45] J. E. McNeal, E. A. Redwine, F. S. Freiha, and T. A. Stamey, "Zonal distribution of prostatic adenocarcinoma – Correlation with histologic pattern and direction of spread", *Am J Surg Pathol*, vol. 12, pp. 897–906, 1988.

[46] A. E. Pelzer, J. Bektic, A. P. Berger, E. J. Halpern, F. Koppelstätter, A. Klauser, P. Rehder, W. Horninger, G. Bartsch, and F. Frauscher, "Are transition zone biopsies still necessary to improve prostate cancer detection? Results from the Tyrol screening project", *Eur Urol*, vol. 48, pp. 916–21; discussion 921, 2005.

[47] E. J. Halpern, "Contrast-enhanced ultrasound imaging of prostate cancer", *Rev Urol*, vol. 8, pp. S29–S37, 2006.

[48] R. C. Flanigan, W. J. Catalona, J. P. Richie, F. R. Ahmann, M. A. Hudson, P. T. Scardino, J. B. deKernion, T. L. Ratliff, L. R. Kavoussi, and B. L. Dalkin, "Accuracy

of digital rectal examination and transrectal ultrasonography in localizing prostate cancer", *J Urol*, vol. 152, pp. 1506–1509, 1994.

[49] W. L. Valk and W. K. Mebust, "The management of the prostatic nodule", *JAMA*, vol. 209, p. 1697, 1969.

[50] J. C. Applewhite, B. R. Matlaga, D. L. McCullough, and M. C. Hall, "Transrectal ultrasound and biopsy in the early diagnosis of prostate cancer", *Cancer Control*, vol. 8, pp. 141–150, 2001.

[51] G. D. Angelis, H. G. Rittenhouse, S. D. Mikolajczyk, L. B. Shamel, and A. Semjonow, "Twenty Years of PSA: From Prostate Antigen to Tumor Marker", *Rev Urol*, vol. 9, pp. 113–123, 2007.

[52] I. M. Thompson, D. K. Pauler, P. J. Goodman, C. M. Tangen, M. S. Lucia, H. L. Parnes, L. M. Minasian, L. G. Ford, S. M. Lippman, E. D. Crawford, J. J. Crowley, and C. A. Coltman, "Prevalence of prostate cancer among men with a prostate-specific antigen level < or = 4.0 ng per milliliter", *N Engl J Med*, vol. 350, pp. 2239–2246, 2004.

[53] G. L. Andriole, R. L. Grubb, S. S. Buys, D. Chia, T. R. Church, M. N. Fouad, E. P. Gelmann, P. A. Kvale, D. J. Reding, J. L. Weissfeld, L. A. Yokochi, E. D. Crawford, B. O'Brien, J. D. Clapp, J. M. Rathmell, T. L. Riley, R. B. Hayes, B. S. Kramer, G. Izmirlian, A. B. Miller, P. F. Pinsky, P. C. Prorok, J. K. Gohagan, C. D. Berg, and P. L. C. O. Project Team, "Mortality results from a randomized prostate-cancer screening trial", *N Engl J Med*, vol. 360, pp. 1310–1319, 2009.

[54] G. Draisma, R. Boer, S. J. Otto, I. W. van der Cruijsen, R. A. M. Damhuis, F. H. Schröder, and H. J. de Koning, "Lead times and overdetection due to prostate-specific antigen screening: estimates from the European Randomized Study of Screening for Prostate Cancer", *J Natl Cancer Inst*, vol. 95, pp. 868–878, 2003.

[55] R. Montironi, R. Mazzuccheli, M. Scarpelli, A. Lopez-Beltran, G. Fellegara, and F. Algaba, "Gleason grading of prostate cancer in needle biopsies or radical prostatectomy specimens: contemporary approach, current clinical significance and sources of pathology discrepancies", *BJU Int*, vol. 95, pp. 1146–1152, 2005.

[56] R. Montironi, R. Mazzucchelli, and T. Kwast, "Morphological assessment of radical prostatectomy specimens. A protocol with clinical relevance", *Virchows Arch*, vol. 442, pp. 211–217, 2003.

[57] M. Seitz, F. Strittmatter, A. Roosen, D. Tilki, and C. Gratzke, "Current status of ultrasound imaging in prostate cancer", *Panminerva Med*, vol. 52, pp. 189–194, 2010.

[58] S. Verma and A. Rajesh, "A clinically relevant approach to imaging prostate cancer: review", *AJR Am J Roentgenol*, vol. 196, pp. S1–S10, 2011.

[59] C. R. Porter, K. Kodama, R. P. Gibbons, R. Correa, F. K.-H. Chun, P. Perrotte, and P. I. Karakiewicz, "25-year prostate cancer control and survival outcomes: a 40-year radical prostatectomy single institution series", *J Urol*, vol. 176, pp. 569–574, 2006.

[60] R. F. Coelho, B. Rocco, M. B. Patel, M. A. Orvieto, S. Chauhan, V. Ficarra, S. Melegari, K. J. Palmer, and V. R. Patel, "Retropubic, laparoscopic, and robot-assisted radical prostatectomy: a critical review of outcomes reported by high-volume centers", *J Endourol*, vol. 24, pp. 2003–2015, 2010.

[61] I. Singh and A. K. Hemal, "Robotic-assisted radical prostatectomy in 2010", *Expert Rev Anticancer Ther*, vol. 10, pp. 671–682, 2010.

[62] T. H. V. der Kwast, M. Bolla, H. V. Poppel, P. V. Cangh, K. Vekemans, L. D. Pozzo, J.-F. Bosset, K. H. Kurth, F. H. Schröder, and L. Collette, "Identification of patients with prostate cancer who benefit from immediate postoperative radiotherapy: EORTC 22911", *J Clin Oncol*, vol. 25, pp. 4178–4186, 2007.

[63] A. N. Vis, F. H. Schröder, and T. H. van der Kwast, "The actual value of the surgical margin status as a predictor of disease progression in men with early prostate cancer", *Eur Urol*, vol. 50, pp. 258–265, 2006.

[64] J. Thoms, J. S. Goda, A. R. Zlotta, N. E. Fleshner, T. H. van der Kwast, S. Supiot, P. Warde, and R. G. Bristow, "Neoadjuvant radiotherapy for locally advanced and high-risk prostate cancer", *Nat Rev Clin Oncol*, vol. 8, pp. 107–113, 2011.

[65] T. Ikeda, *Fundamentals of Piezoelectricity*. Oxford: Oxford University Press, 1990.

[66] F. Mandl, *Statistical Physics*. Chichester: John Wiley & Sons, 2 ed., 1988.

[67] S. Omata and Y. Terunuma, "New tactile sensor like the human hand and its applications", *Sensor Actuat A*, vol. 35, pp. 9–15, 1992.

[68] Y. Murayama and S. Omata, "Fabrication of micro tactile sensor for the measurement of micro-scale local elasticity", *Sensor Actuat A*, vol. 109, pp. 202–207, 2004.

[69] G. Gladwell and C. Kleesattel, "The contact impedance meter I", *Ultrasonics*, vol. 6, pp. 175–180, 1968.

[70] G. Gladwell and C. Kleesattel, "The contact impedance meter II", *Ultrasonics*, vol. 6, pp. 244–252, 1968.

[71] V. Jalkanen, B. M. Andersson, A. Bergh, B. Ljungberg, and O. A. Lindahl, "Explanatory models for a tactile resonance sensor system – elastic and density-related variations of prostate tissue in vitro", *Physiol Meas*, vol. 29, pp. 729–745, 2008.

[72] Y. Murayama, C. E. Constantinou, and S. Omata, "Remote sensing of mechanical properties of materials using a novel ultrasound transducer and signal processing", *IEEE Trans Ultrason Ferroelectr Freq Control*, vol. 52, pp. 439–444, 2005.

[73] Y. Murayama, M. Haruta, Y. Hatakeyama, T. Shiina, H. Sakuma, S. Takenoshita, S. Omata, and C. E. Constantinou, "Development of a new instrument for examination of stiffness in the breast using haptic sensor technology", *Sensor Actuat A*, vol. 143, pp. 430–438, 2008.

[74] V. Jalkanen, "Hand-held resonance sensor for tissue stiffness measurements: a theoretical and experimental analysis", *Meas Sci Technol*, vol. 21, 055801 (8 pp.), 2010.

[75] Y. Murayama, S. Omata, T. Yajima, Q. Peng, K. Shishido, D. M. Peehl, and C. E. Constantinou, "High Resolution Regional Elasticity Mapping of the Human Prostate", in *Proceedings of the 29th Annual International Conference of the IEEE EMBS. Cité Internationale, Lyon, France. August 23-26, 2007*, pp. 5802–5805, 2007.

[76] E. Smith and G. Dent, *Modern Raman Spectroscopy: A Practical Approach*. Chichester: John Wiley & Sons, 2005.

[77] V. Tuchin, *Tissue Optics - Light Scattering Methods and Instruments for Medical Diagnosis*. Bellingham: SPIE Press, 2 ed., 2007.

[78] D. A. Long, "80th Anniversary of the discovery of the Raman Effect: a celebration", *J Raman Spectrosc*, vol. 39, pp. 316–321, 2008.

[79] C. V. Raman and K. S. Krishnan, "A new type of secondary radiation", *Nature*, vol. 121, pp. 501–502, 1928.

[80] J. R. Ferraro, K. Nakamoto, and C. W. Brown, *Introductory Raman Spectroscopy*. San Diego: Academic Press, 2 ed., 2003.

[81] A. Mahadevan-Jansen and R. R. Richards-Kortum, "Raman spectroscopy for the detection of cancers and precancers", *J Biomed Opt*, vol. 1, pp. 31–70, 1996.

[82] G. Pitt, D. Batchelder, R. Bennett, R. Bormett, I. Hayward, B. Smith, K. Williams, Y. Yang, K. Baldwin, and S. Webster, "Engineering aspects and applications of the new Raman instrumentation", *IEE Proc-Sci Meas Technol*, vol. 152, pp. 241–318, 2005.

[83] E. B. Hanlon, R. Manoharan, T.-W. Koo, K. E. Shafer, J. T. Motz, M. Fitzmaurice, J. R. Kramer, I. Itzkan, R. R. Dasari, and M. S. Feld, "Topical review: prospects for in vivo Raman spectroscopy", *Phys Med Biol*, vol. 45, pp. R1–R59, 2000.

[84] J. C. C. Day, R. Bennett, B. Smith, C. Kendall, J. Hutchings, G. M. Meaden, C. Born, S. Yu, and N. Stone, "A miniature confocal Raman probe for endoscopic use", *Phys Med Biol*, vol. 54, pp. 7077–7087, 2009.

[85] C. Kendall, J. Day, J. Hutchings, B. Smith, N. Shepherd, H. Barr, and N. Stone, "Evaluation of Raman probe for oesophageal cancer diagnostics", *Analyst*, vol. 135, pp. 3038–3041, 2010.

[86] S. Koljenović, T. C. B. Schut, R. Wolthuis, B. de Jong, L. Santos, P. J. Caspers, J. M. Kros, and G. J. Puppels, "Tissue characterization using high wave number Raman spectroscopy", *J Biomed Opt*, vol. 10, 031116 (11 pp.), 2005.

[87] L. F. Santos, R. Wolthuis, S. Koljenović, R. M. Almeida, and G. J. Puppels, "Fiber-optic probes for in vivo Raman spectroscopy in the high-wavenumber region", *Anal Chem*, vol. 77, pp. 6747–6752, 2005.

[88] S. Koljenović, T. C. B. Schut, R. Wolthuis, A. J. P. E. Vincent, G. Hendriks-Hagevi, L. Santos, J. M. Kros, and G. J. Puppels, "Raman spectroscopic characterization of porcine brain tissue using a single fiber-optic probe", *Anal Chem*, vol. 79, pp. 557–564, 2007.

[89] Y. Komachi, H. Sato, K. Aizawa, and H. Tashiro, "Micro-optical fiber probe for use in an intravascular Raman endoscope", *Appl Opt*, vol. 44, pp. 4722–4732, 2005.

[90] Y. Komachi, H. Sato, and H. Tashiro, "Intravascular Raman spectroscopic catheter for molecular diagnosis of atherosclerotic coronary disease", *Appl Opt*, vol. 45, pp. 7938–7943, 2006.

[91] Y. Komachi, T. Katagiri, H. Sato, and H. Tashiro, "Improvement and analysis of a micro Raman probe", *Appl Opt*, vol. 48, pp. 1683–1696, 2009.

[92] Y. Hattori, Y. Komachi, T. Asakura, T. Shimosegawa, G.-I. Kanai, H. Tashiro, and H. Sato, "In vivo Raman study of the living rat esophagus and stomach using a micro-Raman probe under an endoscope", *Appl Spectrosc*, vol. 61, pp. 579–584, 2007.

[93] N. Stone and P. Matousek, "Advanced transmission Raman spectroscopy: a promising tool for breast disease diagnosis", *Cancer Res*, vol. 68, pp. 4424–4430, 2008.

[94] H. Edwards and E. Carter, "Biological Applications of Raman Spectroscopy", in *Infrared and Raman Spectroscopy of Biological Materials* (H.-U. Gremlich and B. Yan, eds.), vol. 24 of *Practical Spectroscopy*, ch. 11, New York: Marcel Dekker, 2001.

[95] L. C. Kwek, S. Fu, T. C. Chia, C. H. Diong, C. L. Tang, and S. M. Krishnan, "High-sensitivity and specificity of laser-induced autofluorescence spectra for detection of colorectal cancer with an artificial neural network", *Appl Opt*, vol. 44, pp. 4004–4008, 2005.

[96] C. A. Lieber and A. Mahadevan-Jansen, "Automated method for subtraction of fluorescence from biological Raman spectra", *Appl Spectrosc*, vol. 57, pp. 1363–1367, 2003.

[97] A. Cao, A. K. Pandya, G. K. Serhatkulu, R. E. Weber, H. Dai, J. S. Thakur, V. M. Naik, R. Naik, G. W. Auner, R. Rabah, and D. C. Freeman, "A robust method for automated background subtraction of tissue fluorescence", *J Raman Spectrosc*, vol. 38, pp. 1199–1205, 2007.

[98] Z. Movasaghi, S. Rehman, and I. Rehman, "Raman spectroscopy of biological tissues", *Appl Spectrosc Rev*, vol. 42, pp. 493–541, 2007.

[99] A. Taleb, J. Diamond, J. J. McGarvey, J. R. Beattie, C. Toland, and P. W. Hamilton, "Raman microscopy for the chemometric analysis of tumor cells", *J Phys Chem B*, vol. 110, pp. 19625–19631, 2006.

[100] N. Stone, C. Kendall, N. Shepherd, P. Crow, and H. Barr, "Near-infrared Raman spectroscopy for the classification of epithelial pre-cancers and cancers", *J Raman Spectrosc*, vol. 33, pp. 564–573, 2002.

[101] P. Crow, A. Ritchie, M. Wright, C. Kendall, and N. Stone, "Evaluation of Raman spectroscopy to provide a real time optical method for discrimination between normal and abnormal tissue in the prostate", *Eur Urol Suppl*, vol. 1, p. 92, 2002.

[102] M. G. Shim and B. C. Wilson, "The effects of ex vivo handling procedures on the near-infrared Raman spectra of normal mammalian tissues", *Photochem Photobiol*, vol. 63, pp. 662–671, 1996.

[103] C. M. Krishna, G. D. Sockalingum, B. M. Vadhiraja, K. Maheedhar, A. C. K. Rao, L. Rao, L. Venteo, M. Pluot, D. J. Fernandes, M. S. Vidyasagar, V. B. Kartha, and M. Manfait, "Vibrational spectroscopy studies of formalin-fixed cervix tissues", *Biopolymers*, vol. 85, pp. 214–221, 2007.

[104] C. M. Krishna, G. D. Sockalingum, L. Venteo, R. A. Bhat, P. Kushtagi, M. Pluot, and M. Manfait, "Evaluation of the suitability of ex vivo handled ovarian tissues for optical diagnosis by Raman microspectroscopy", *Biopolymers*, vol. 79, pp. 269–276, 2005.

[105] E. O Faolain, M. B. Hunter, J. M. Byrne, P. Kelehan, M. McNamara, H. J. Byrne, and F. M. Lyng, "A study examining the effects of tissue processing on human tissue sections using vibrational spectroscopy", *Vib Spectrosc*, vol. 38, pp. 121–127, 2005.

[106] N. Boustany, J. Crawford, R. Manoharan, R. Dasari, and M. Feld, "Effects of freeze-thaw and photobleaching on the ultraviolet resonance Raman spectra of human colon biopsies", *Appl Spectrosc*, vol. 55, pp. 1506–1513, 2001.

[107] K. C. Neuman, E. H. Chadd, G. F. Liou, K. Bergman, and S. M. Block, "Characterization of photodamage to escherichia coli in optical traps", *Biophys J*, vol. 77, pp. 2856–2863, 1999.

[108] I. Notingher, S. Verrier, H. Romanska, A. Bishop, J. Polak, and L. Hench, "In situ characterisation of living cells by Raman spectroscopy", *Spectroscopy*, vol. 16, pp. 43–51, 2002.

[109] G. J. Puppels, J. H. Olminkhof, G. M. Segers-Nolten, C. Otto, F. F. de Mul, and J. Greve, "Laser irradiation and Raman spectroscopy of single living cells and chromosomes: sample degradation occurs with 514.5 nm but not with 660 nm laser light", *Exp Cell Res*, vol. 195, pp. 361–367, 1991.

[110] R. W. Chan and I. R. Titze, "Effect of postmortem changes and freezing on the viscoelastic properties of vocal fold tissues", *Ann Biomed Eng*, vol. 31, pp. 482–491, 2003.

[111] M. Szarko, K. Muldrew, and J. E. Bertram, "Freeze-thaw treatment effects on the dynamic mechanical properties of articular cartilage", *BMC Musculoskelet Disord*, vol. 11, 231 (8 pp.), 2010.

[112] S. Krag and T. T. Andreassen, "Effect of freezing on lens capsule mechanical behavior", *Ophthalmic Res*, vol. 30, pp. 280–285, 1998.

[113] T. Oie, H. Suzuki, T. Fukuda, Y. Murayama, S. Omata, K. Kanda, and Y. Nakayama, "Tactile Mapping System: A Novel Imaging Technology for Surface Topography and Elasticity of Tissues or Organs", *Innovations*, vol. 4, pp. 345–350, 2009.

[114] T. Oie, Y. Murayama, T. Fukuda, C. Nagai, S. Omata, K. Kanda, H. Yaku, and Y. Nakayama, "Local elasticity imaging of vascular tissues using a tactile mapping system", *J Artif Organs*, vol. 12, pp. 40–46, 2009.

[115] T. Oie, H. Suzuki, Y. Murayama, T. Fukuda, S. Omata, K. Kanda, K. Takamizawa, and Y. Nakayama, "Surface elasticity imaging of vascular tissues in a liquid environment by a scanning haptic microscope", *J Artif Organs*, vol. 13, pp. 121–125, 2010.

[116] R. A. Johnson and D. W. Wichern, *Applied Multivariate Statistical Analysis*. Upper Saddle River: Prentice-Hall, 4 ed., 1998.

[117] M. Romeo and M. Diem, "Infrared spectral imaging of lymph nodes: Strategies for analysis and artifact reduction", *Vib Spectrosc*, vol. 38, pp. 115–119, 2005.

[118] C. Cortes and V. Vapnik, "Support-Vector Networks", *Machine Learning*, vol. 20, pp. 273–297, 1995.

[119] Y.-W. Chen and C.-J. Lin, "Combining SVMs with Various Feature Selection Strategies", in *Feature Extraction* (I. Guyon, M. Nikravesh, S. Gunn, and L. Zadeh, eds.), vol. 207 of *Studies in Fuzziness and Soft Computing*, pp. 315–324, Springer Berlin / Heidelberg, 2006.

[120] C.-W. Hsu and C.-J. Lin, "A Comparison of Methods for Multiclass Support Vector Machines", *IEEE T Neural Networ*, vol. 13, pp. 415–425, 2002.

[121] M. Sattlecker, C. Bessant, J. Smith, and N. Stone, "Investigation of support vector machines and Raman spectroscopy for lymph node diagnostics", *Analyst*, vol. 135, pp. 895–901, 2010.

[122] E. Widjaja, W. Zheng, and Z. Huang, "Classification of colonic tissues using near-infrared Raman spectroscopy and support vector machines", *Int J Oncol*, vol. 32, pp. 653–662, 2008.

[123] S. K. Majumder, N. Ghosh, and P. K. Gupta, "Support vector machine for optical diagnosis of cancer", *J Biomed Opt*, vol. 10, 024034 (14 pp.), 2005.

[124] Y. Murayama, C. Constantinou, and S. Omata, "Development of Tactile Mapping system for the stiffness characterization of tissue slice using novel tactile sensing technology", *Sensor Actuat A*, vol. 120, pp. 543–549, 2005.

[125] Y. Murayama and S. Omata, "Considerations in the design and sensitivity optimization of the micro tactile sensor", *IEEE Trans Ultrason Ferroelectr Freq Control*, vol. 52, pp. 434–438, 2005.

[126] P. H. Eilers, "A perfect smoother", *Anal Chem*, vol. 75, pp. 3631–3636, 2003.

[127] Y. L. Loethen, D. Zhang, R. N. Favors, S. B. G. Basiaga, and D. Ben-Amotz, "Second-derivative variance minimization method for automated spectral subtraction", *Appl Spectrosc*, vol. 58, pp. 272–278, 2004.

[128] S. Kim, "A practical solution to the multivariate Behrens-Fisher problem", *Biometrika*, vol. 79, pp. 171–176, 1992.

[129] L. M. Lix, H. J. Keselman, and A. M. Hinds, "Robust tests for the multivariate Behrens-Fisher problem", *Comput Methods Programs Biomed*, vol. 77, pp. 129–139, 2005.

[130] K. K. Yuen, "The two-sample trimmed t for unequal population variances", *Biometrika*, vol. 61, pp. 165–171, 1974.

[131] S. W. T. P. J. Heijmink, H. van Moerkerk, L. A. L. M. Kiemeney, J. A. Witjes, F. Frauscher, and J. O. Barentsz, "A comparison of the diagnostic performance of systematic versus ultrasound-guided biopsies of prostate cancer", *Eur Radiol*, vol. 16, pp. 927–938, 2006.

[132] L. Pallwein, M. Mitterberger, J. Gradl, F. Aigner, W. Horninger, H. Strasser, G. Bartsch, D. zur Nedden, and F. Frauscher, "Value of contrast-enhanced ultra-sound and elastography in imaging of prostate cancer", *Curr Opin Urol*, vol. 17, pp. 39–47, 2007.

[133] J. Kurhanewicz, D. Vigneron, P. Carroll, and F. Coakley, "Multiparametric magnetic resonance imaging in prostate cancer: present and future", *Curr Opin Urol*, vol. 18, pp. 71–77, 2008.

[134] P. Wang, Y. min Guo, M. Liu, Y. qian Qiang, X. juan Guo, Y. li Zhang, X.-Y. Duan, Q.-J. Zhang, and W. Liang, "A meta-analysis of the accuracy of prostate cancer studies which use magnetic resonance spectroscopy as a diagnostic tool", *Korean J Radiol*, vol. 9, pp. 432–438, 2008.

[135] M. Chen, H.-D. Dang, J.-Y. Wang, C. Zhou, S.-Y. Li, W.-C. Wang, W.-F. Zhao, Z.-H. Yang, C.-Y. Zhong, and G.-Z. Li, "Prostate cancer detection: comparison of T2-weighted imaging, diffusion-weighted imaging, proton magnetic resonance spectroscopic imaging, and the three techniques combined", *Acta Radiol*, vol. 49, pp. 602–610, 2008.

[136] T. Hambrock, J. J. Fuetterer, H. J. Huisman, C. Hulsbergen-vandeKaa, J.-P. van Basten, I. van Oort, J. A. Witjes, and J. O. Barentsz, "Thirty-two-channel coil 3T magnetic resonance-guided biopsies of prostate tumor suspicious regions identified on multimodality 3T magnetic resonance imaging: Technique and feasibility", *Invest Radiol*, vol. 43, pp. 686–694, 2008.

[137] T. Tamada, T. Sone, Y. Jo, A. Yamamoto, T. Yamashita, N. Egashira, S. Imai, and M. Fukunaga, "Prostate cancer: relationships between postbiopsy hemorrhage and tumor detectability at MR diagnosis", *Radiology*, vol. 248, pp. 531–539, 2008.

[138] K. J. Macura, "Multiparametric magnetic resonance imaging of the prostate: current status in prostate cancer detection, localization, and staging", *Semin Roentgenol*, vol. 43, pp. 303–313, 2008.

[139] J. M. Berg, J. L. Tymoczko, and L. Stryer, *Biochemistry*. New York: Freeman, 5 ed., 2002.

Part II

Paper A

Technologies for localization and diagnosis of prostate cancer

Authors:
Stefan Candefjord, Kerstin Ramser and Olof A. Lindahl

---

[1]http://dx.doi.org/10.3109/03091900903111966

Paper B

Effects of snap-freezing and near-infrared laser illumination on porcine prostate tissue as measured by Raman spectroscopy

Authors:
Stefan Candefjord, Kerstin Ramser and Olof A. Lindahl

---

[1]http://dx.doi.org/10.1039/b820931f

Combining fibre optic Raman spectroscopy and tactile resonance measurement for tissue characterization

Authors:

Stefan Candefjord, Morgan Nyberg, Ville Jalkanen, Kerstin Ramser and Olof A. Lindahl

---

[1]`http://dx.doi.org/10.1088/0957-0233/21/12/125801`

Paper D

Combining scanning haptic microscopy and fiber optic Raman spectroscopy for tissue characterization

Authors:
Stefan Candefjord, Yoshinobu Murayama, Morgan Nyberg, Josef Hallberg, Kerstin Ramser, Börje Ljungberg, Anders Bergh and Olof A. Lindahl